

LeLaR: The First In-Orbit Demonstration of an AI-Based Satellite Attitude Controller

Kirill Djebko^{a,b,*}, Tom Baumann^b, Erik Dilger^b, Frank Puppe^a,
Sergio Montenegro^b

^a*Julius-Maximilians-Universität Würzburg, Center for Artificial Intelligence and Data Science, Emil-Fischer-Straße 50, 97074, Würzburg, Germany*

^b*Julius-Maximilians-Universität Würzburg, Chair of Computer Science VIII - Aerospace Information Technology, Emil-Fischer-Straße 70, 97074, Würzburg, Germany*

Abstract

Attitude control is essential for many satellite missions. Classical controllers, however, are time-consuming to design and sensitive to model uncertainties and variations in operational boundary conditions. Deep Reinforcement Learning (DRL) offers a promising alternative by learning adaptive control strategies through autonomous interaction with a simulation environment. Overcoming the Sim2Real gap, which involves deploying an agent trained in simulation onto the real physical satellite, remains a significant challenge. In this work, we present the first successful in-orbit demonstration of an AI-based attitude controller for inertial pointing maneuvers. The controller was trained entirely in simulation and deployed to the InnoCube 3U nanosatellite, which was developed by the Julius-Maximilians-Universität Würzburg in cooperation with the Technische Universität Berlin, and launched in January 2025. We present the AI agent design, the methodology of the training procedure, the discrepancies between the simulation and the observed behavior of the real satellite, and a comparison of the AI-based attitude controller with the classical PD controller of InnoCube. Steady-state metrics confirm the robust performance of the AI-based controller during repeated in-orbit maneuvers.

Keywords: Artificial Intelligence, Attitude Control, CubeSats, Deep Reinforcement Learning, In-Orbit Demonstration, Nanosatellites

*Corresponding author

Email address: kirill.djebko@uni-wuerzburg.de (Kirill Djebko)

1. Introduction and Background

In recent years, Machine Learning (ML) and Artificial Intelligence (AI)-based methods have increasingly entered engineering disciplines, particularly robotics, with notable progress in quadrupedal [1] and humanoid robots such as Agile Justin developed at the German Aerospace Center (DLR) [2]. This influence is now expanding into the aerospace sector, where AI-driven methods are being explored for highly nonlinear applications, including robust attitude control for launch vehicles [3, 4], combustion chamber regulation [5], UAV control [6, 7], and satellite attitude control [8, 9, 10].

The motivation stems from the increasing autonomy and complexity required by modern spacecraft, which demand control strategies capable of adapting to dynamic environments while minimizing human intervention. Deep Reinforcement Learning (DRL), a variant of classical Reinforcement Learning [11], has shown considerable promise in this context. For example, for launch vehicles, DRL-based controllers using the Soft Actor-Critic [12] algorithm have been applied in simulation to achieve load-relief attitude control under aerodynamic disturbances [3]. Similarly, DRL-based adaptive controllers for quad-tiltrotor UAVs improve disturbance rejection and tracking performance compared to classical methods [6] in simulation.

For satellites, DRL has been used in simulation to maintain operational capability under unknown ADCS failures, where a Deep Deterministic Policy Gradient (DDPG) [13]-based controller reorients solar panels toward the Sun without requiring explicit fault models [8]. Other work demonstrates the feasibility of real-time DRL-based magnetic attitude control on embedded hardware on ground [9]. In addition, Proximal Policy Optimization (PPO) [14]-based controllers using stacked observations, similar to our observation space design from [15], achieve robust attitude control across varying satellite masses in simulation, outperforming classical PID control in settling time and stability [10]. The Hybrid Online Policy Adaptation Strategy (HOPAS) project attempted an early in-orbit demonstration of a Reinforcement Learning-based attitude controller on the ESA OPS-SAT CubeSat, with the AI agent designed to modify the PID control signals as a residual command, but the full AI closed-loop control was ultimately restricted to simulation and ground-testing [16, 17]. These developments illustrate the growing interest in DRL and AI-based control methods for aerospace systems

characterized by nonlinear dynamics and uncertainties.

To date AI-based attitude control has been restricted to simulation environments or laboratory testbeds, with no successful in-orbit demonstrations. This work represents the first successful test of an AI-based attitude controller in orbit.

Building on our previous works [15, 18, 19], we developed an AI-based attitude controller for the InnoCube 3U nanosatellite [20, 21, 22], developed by the Julius-Maximilians-Universität Würzburg and the Technische Universität Berlin, which successfully launched on January 14, 2025. The AI agent autonomously interacts with a simulated environment to learn a control strategy that maximizes a given reward function. The agent was first trained on a basic control task to obtain a base-agent, which was subsequently post-trained to produce the final flight-agent. The controller was trained entirely on ground, uploaded to InnoCube, and tested in orbit. Since the present work was done as part of the “In-Orbit Demonstrator Learning Attitude Control” (German: In-Orbit-Demonstrator Lernende Lageregelung; LeLaR) project, we also refer to the AI agent as LeLaR. The InnoCube project is funded by the Federal Ministry for Economic Affairs and Energy (BMWE) under grant number (FKZ) 50RU2000.

A disadvantage of DRL lies in the tendency of neural networks to achieve good results in interpolation tasks but failure in extrapolation problems [23]. In that sense, the process of transferring an AI agent trained in simulation to the real target system is called Sim2Real transfer and poses a significant challenge when applying DRL to real-world tasks. For practical applications, it is necessary to vary the boundary conditions during training, e.g., via domain randomization, to avoid so-called Out-of-Distribution errors. This includes, in particular, the moments of inertia, which we have already successfully considered in [15, 18] and utilize in this work.

While originally a pure reaction wheel control was planned, an unexpected limitation regarding the reaction wheel speeds emerged prior to the launch of InnoCube. Operation of the wheels in the range of $[-350, 350]$ rpm should be avoided, as this can lead to inaccurate wheel speed estimation and control. As a precautionary measure, we have therefore split the agent network into a reaction wheel (RW) subnetwork and a magnetorquer (MT) subnetwork and integrated momentum management using the latter. During initial tests in orbit, several operational constraints limited our planned approach. In the early experiment phase, command list execution was not available, limiting tests to live teleoperation during passes. These passes, with a maximum

duration of approximately 12 minutes, were too short to conduct complete momentum management tests and prompted us to consider the RW sub-network in isolation. During these tests however, it became apparent, that the RW subnetworks performance alone was sufficient and also fit the later safety and power constraint of a maximum experiment duration of 15 minutes after unsupervised command execution became available. Subsequently we used the RW subnetwork from the original agent as base-agent and adapted it to the remaining operational requirement changes by finetuning through post-training as we line out in Section 2.6.

This paper is structured as follows: In Section 2, we first introduce the InnoCube satellite and the InnoCube simulation model. We then present the observation and action space, the performed calibration and the training of the base- and flight-agent. Finally, we present the Safety Cage in which the attitude controllers are embedded and the integration into the InnoCube satellite. In Section 3, we briefly discuss the discrepancies observed between the simulated behavior and the actual in-orbit performance of the satellite and provide in-orbit experiments for these discrepancies. We then present the performance of the AI-based attitude controller based on steady-state metrics and compare it to the InnoCube’s default PD controller. In Section 4, we discuss our results and give an outlook on future work.

2. Methodology

The following sections outline the components required to apply DRL to the attitude control task. This involves developing a simulation model of the target system, defining the observation space as the AI agent’s inputs and the action space as its outputs, and specifying an appropriate optimization target. This optimization target, the so-called reward function, together with the observation space, form the core components of the DRL procedure. For training we follow an iterative approach by first training a base-agent that learns to solve the basic attitude control problem and which is then post-trained to handle more complicated boundary conditions, augmented by noise and disturbances.

As base-agent, we employ the post-trained agent from our prior work [24], using a split policy network, consisting of a reaction wheel and a magnetorquer subnetwork. It was originally designed to avoid prolonged RW operation in the interval of $[-350, 350]$ rpm to avoid the inaccuracies stemming from the RWs rate estimator when operated in this range. Initial tests in-orbit

however revealed that the RW subnetwork alone performed sufficient well, as we will discuss in Section 3. Along with changed safety requirements introduced after deployment but prior to the first test, this observation prompted us to use the RW subnetwork of the agent from [24] as base and to fine tune it through post-training for standalone use. We refer to the post-trained agent as LeLaR flight-agent or flight-agent in short.

Since [24] is available only in German, we adapt and summarize the essential elements required to understand the current work and expand on important aspects. This includes the base-agent design and the sensor calibration methodology adapted from our prior work, covering both the physical on-board sensors and the simulation environment used for training of all agents. It is to be noted, that sensor calibration is not a requirement introduced by the DRL procedure but should generally be performed for any satellite mission. It is included here for completeness, as calibration affects both the satellite’s sensors and the quality of the simulation. We then highlight the modifications to the model and reward function, as well as the updated operational requirements and boundary conditions, applied to obtain the flight-agent. Finally, the Safety Cage architecture is described, encompassing the AI agent to ensure safe and reliable operation in case of a fault.

2.1. InnoCube Satellite

InnoCube is a 3U CubeSat mission designed as a technology demonstrator for several innovative technologies and has successfully been launched on January 14, 2025 into a 520km sun-synchronous orbit. InnoCube carries two main experiments: “Skip The Harness” (SKITH), a fully wireless data bus for intra-satellite communication and “Fibre-Reinforced Spacecraft Wall for Storing Energy” (Wall#E), an experimental carbon fiber reinforced plastic solid-state battery. Secondary payloads include amateur radio payloads and the “Experiment for Precise Orbit Determination” (EPISODE) experiment, a software defined GNSS receiver. InnoCube is a collaborative effort between the Julius-Maximilians-Universität Würzburg and the Technische Universität Berlin [22]. The InnoCube satellite is a 3U CubeSat with a mass of 4.2 kg. An overview of the spacecraft’s subsystems is provided in Figure 1.

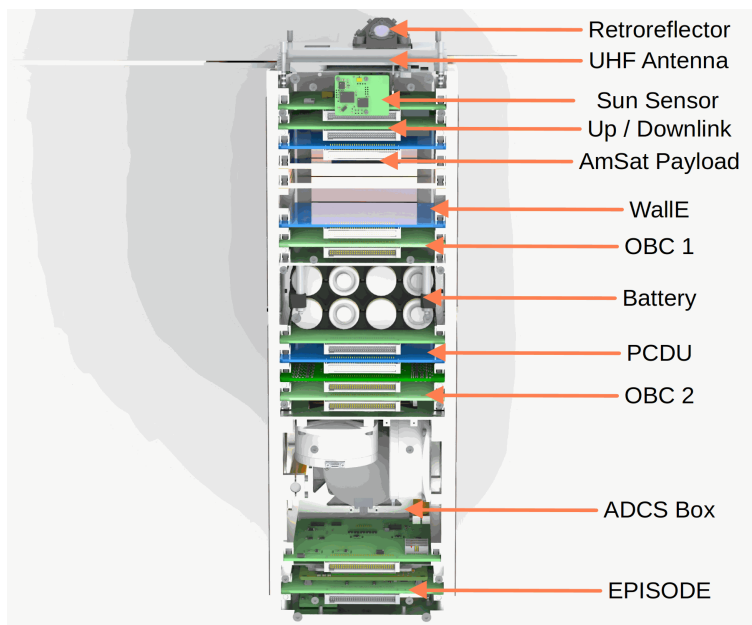


Figure 1: Overview of the components of the InnoCube satellite.

Communication with the ground station is established via a UHF operating in the 433 MHz amateur radio band. Electrical power is generated by four 3U solar panels mounted on the long sides of the satellite and is stored in a 12 Ah battery.

On-board data handling is distributed across the satellite's individual hardware nodes. The system is based on the Silicon Labs EFR32FG12 microcontroller, which features an ARM Cortex-M4 processor [25]. It integrates a 2.4 GHz RF front end that serves as the foundation for the wireless bus system Skip-the-Harness (SKITH). All spacecraft modules share this wireless data interface. Mission-critical bus functions are implemented within the PCDU, the COM node and the OBC node. These include power management, telemetry and telecommand functionality, as well as general bus operations.

The Attitude Determination and Control System (ADCS) is housed within a dedicated sub-assembly (ADCS-Box). It comprises the cold-redundant ADCS mainboard (including gyro and magnetometer sensors), three magnetorquers with dual redundancy along all axes (ferrite-core coils) and three reaction wheels. Sun sensors mounted on the exterior of the satellite provide external sensing and are connected wirelessly to the ADCS mainboard.

2.1.1. *InnoCube* ADCS

The ADCS for InnoCube had been developed mainly from requirements derived from the EPISODE payload, which did not pose highly sophisticated constraints on the performance requirements for the ADCS. Two main modes had been considered: GNSS Pointing and Laser-Ranging Tracking. GNSS Pointing requires the GNSS Antennas to be pointed away from the earth, providing unobstructed view for the antennas to GNSS satellites. This resulted in a very low pointing requirement of around plus minus 90° of anti nadir pointing. Laser-Ranging Tracking requires the retroreflector to be pointed towards the laser-ranging ground station with a pointing accuracy of $\pm 17^\circ$ during a ground station pass.

The LeLaR project, as part of which the present work was conducted, had started after the design of the InnoCube satellite had been completed. Therefore, design requirements resulting from LeLaR could only be based on the existing system built for the InnoCube mission.

As previously mentioned in Section 2.1, all spacecraft modules share the same EFR32FG12 microcontroller. On the ADCS mainboard, the basic circuitry of the microcontroller is extended to accommodate the electrical components needed for the ADCS. These include the gyroscope, the magnetometer, controllers and electrical interfaces for the magnetorquers, electrical interfaces to the reaction wheels and other necessary electrical systems. The used gyroscope to measure the body rates of the satellite is a STMicroelectronics ASM330LHH micro-electromechanical systems (MEMS) gyro [26]. The used magnetometer to measure the magnetic vector with respect to the body frame is a three-axis PNI RM3100 magneto-inductive sensor [27]. The external sun sensors are not used for the current LeLaR experiments, since we currently only determine the relative attitude using a quaternion integrator based on the measured gyro body rates.

Since InnoCube lacks highly accurate absolute determination sensors (e.g., star-trackers) and the accuracy of the sensor fusion utilizing magnetometer and sun-sensor measurements currently does not produce accurate continuous determination-solutions, the in-orbit data relies on gyro measurements only. This also has the advantage, that the evaluation of control accuracy will only be affected by the accuracy of the gyro integration. Since the current analysis focuses on relative control performance only and control maneuvers are conducted in a relatively short time period, absolute attitude knowledge is not necessary for this evaluation.

The sensor calibration had been done in two stages: Laboratory data had been collected prior to launch and used to calibrate gyro and magnetometer data. The gyro bias had been calibrated in-orbit using the method described in Section 2.4 to further increase accuracy. The magnetometer hard- and soft-iron compensation had also been recalculated using in-orbit data.

InnoCube uses two actuator types for controlling attitude: reaction wheels and ferrite-core magnetorquers. Both actuators are placed in an orthogonal configuration aligned with the principle axes of the satellite. Reaction wheels are used for changing the attitude while the magnetorquers are used for wheel momentum management and detumbling during and after a maneuver. The used RWs offer a maximum torque of 2 mNm per axis and a total maximum angular momentum of 30 mNms per axis. Details on the reaction wheel behaviour in-orbit will be discussed in Section 3.2.1. The ferrite-core MTs allow for a maximum commandable dipole moment of approximately $\pm 0.35 \text{ Am}^2$ in all axes. The InnoCube ADCS specifications can be found in Table 1.

Table 1: InnoCube ADCS specifications.

Component	Value	Specifications
Computing Unit	SL EFR32FG12	40 MHz, 1024 kB Flash
	ARM-Cortex M4	256 kB RAM
Gyroscope	ST ASM330LHH	$1.41 \times 10^{-4} \text{ rad/s}$
Magnetometer	PNI RM3100	$5.1 \times 10^{-3} \mu \text{ T}$
Reaction Wheels	3 x orthogonal RW	max. 2 mNm, 30 mNms
Magnetorquer	3 x Ferrite-Core Torquers	0.35 Am^2 orthogonal
Determination Algorithm	Relative rates integration	
ADCS Loop Frequency	1 Hz	

2.1.2. InnoCube ADCS software

The InnoCube ADCS software is constructed in a modular manner. Figure 2 depicts the different software components.

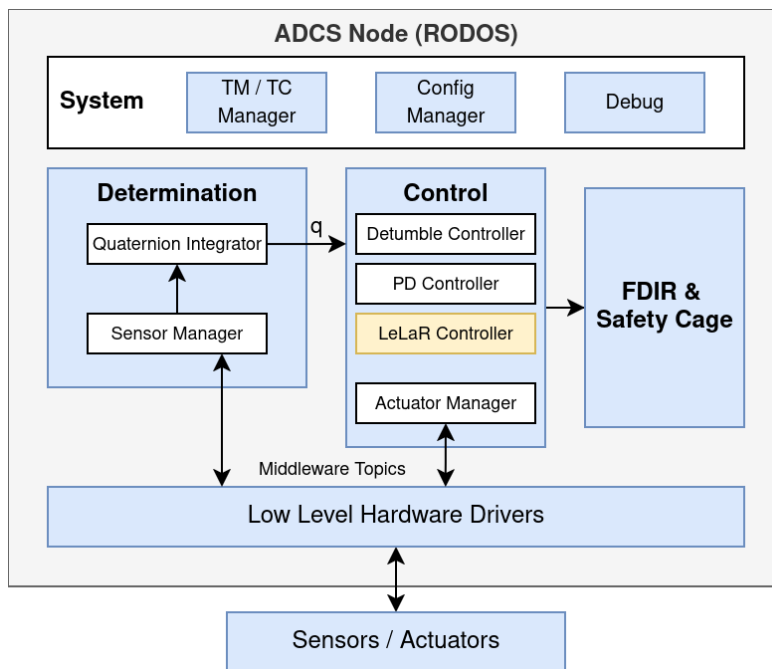


Figure 2: ADCS Software Modules.

The software runs on the on-board operating system RODOS. The determination module collects data from the low-level hardware drivers, which connect to the sensors. In nominal operation, the sensor data along with model data is fused into an absolute attitude solution. Because the LeLaR experiments currently focus only on control performance and not on overall system performance (which includes determination performance), the relative attitude is estimated only using gyro rate integration in the quaternion integrator module. The determination module outputs a calculated attitude quaternion along with the current satellite body rates. This information, together with all current sensor values, is forwarded into the controller module, which can host several control algorithms. Along with a commanded attitude, the control module calculates a control command, which is then forwarded to the satellites actuators. Fault detection isolation and recovery (FDIR) as well as the Safety Cage architecture (see Section 2.7.1) run in parallel in a separate module. The whole ADCS loop runs with a frequency of 1 Hz.

2.1.3. InnoCube PD controller

For inertial pointing maneuvers, a classical proportional-derivative (PD) controller based on the following control law has been implemented serving as the main controller for the original InnoCube mission.

We consider the current attitude quaternion q which maps a vector from the inertial reference frame into the satellite-fixed body frame. Along with a commanded constant target quaternion q_t we define the current attitude error quaternion as

$$\delta q = \begin{bmatrix} \delta q_s \\ \delta q_v \end{bmatrix} = q_t^{-1} \odot q \quad (1)$$

where $\delta q_s = \delta q_0$ is the scalar part of the attitude error quaternion, $\delta q_v = [\delta q_1, \delta q_2, \delta q_3]^T$ denotes its vector part and \odot is the Hamilton quaternion product. The commanded reaction wheel acceleration τ_{rw} is defined using the following control law:

$$\tau_{rw} = -k_p \text{sign}(\delta q_s) \delta q_v - k_d (1 + \delta q_v^T \delta q_v) \omega \quad (2)$$

where ω is the rotational rate vector in the satellite body frame in radians per second. The proportional gain is defined as the vector k_p

$$k_p = \begin{bmatrix} k_p \\ k_p \\ k_p z_{\text{axis scale}} \end{bmatrix} \quad (3)$$

and analogous the derivative gain as the vector k_d

$$k_d = \begin{bmatrix} k_d \\ k_d \\ k_d z_{\text{axis scale}} \end{bmatrix} \quad (4)$$

The k_d and k_p parameters are positive scalar gains of $k_p = 670$ and $k_d = 2500$. The PD controller gain values have been manually derived and tuned using a similar simulation setup to that used for LeLaR. No particular emphasis on high controller performance had been placed on the controller, given the requirements as mentioned in Section 2.1.1.

The Z-axis scale is approximated using the ratio of the principal inertial moments of the Z-axis with respect to the X-axis of the satellite. This factor approximates to around 0.2, which has been used to scale the Z-axis torque correspondingly.

The PD controller had already been in use prior to the LeLaR experiments on-board of InnoCube and was developed independently from LeLaR.

2.2. Simulation Model

A simulation model of the InnoCube satellite was built using component specifications, CAD-based inertia estimates, and experimental subsystem data. Table 2 lists the key model parameters relevant to the dynamics of the model.

Table 2: Key model parameters relevant to the dynamics of the model.

Parameter	Value
Sat. Inertia	$[4.28, 4.22, 0.985] \times 10^{-2} \text{ kg}\cdot\text{m}^2$
RW max Omega	$[1.64, 1.64, 1.64] \times 10^4 \text{ rpm}$
RW Inertia	$[5.68, 5.68, 5.68] \times 10^{-5} \text{ kg}\cdot\text{m}^2$
RW min Torque	$[1.0, 1.0, 1.0] \times 10^{-5} \text{ Nm}$
RW max Torque	$[2.0, 2.0, 2.0] \times 10^{-3} \text{ Nm}$

The simulated orbit is based on InnoCube TLE data from CelesTrak [28], with variations applied during training. Table 3 summarizes nominal values and offsets.

Table 3: Overview of orbit parameters and their variations.

Parameter	Value	Variation (offset)
Perigee	508 km	$U \sim (-5, 5) \text{ km}$
Apogee	519 km	$U \sim (-5, 5) \text{ km}$
Eccentricity	7.630×10^{-4}	$U \sim (-1\text{e-}4, 3\text{e-}4)$
Inclination	97.43°	$U \sim (-0.03, 0.03)^\circ$
RAAN	$U \sim (0, 360)^\circ$	
Arg. of Perigee	$U \sim (0, 360)^\circ$	
True Anomaly	$U \sim (0, 360)^\circ$	

Observations and actions are computed at 1 Hz, while system dynamics are simulated at 10 Hz.

2.3. Observation and Action Space

The observation space is defined as a 39-dimensional vector, normalized to $[-1, 1]$. The action space of the base-agent (see Section 2.5) has 6 elements: three RW torque commands and three MT dipole commands. The

action space of the flight-agent (RW subnetwork; see Section 2.6) is subsequently the three RW torque commands. The agent output values are in the interval of $[-1, 1]$. To obtain the effective action the agent outputs have to be scaled by the maximum RW torque or maximum dipole moment of the respective actuator. Table 4 shows the different components of the AI agents observation space.

Table 4: Features of the observation space.

Component	Length	Description	Time
<i>err_quat</i>	4	Attitude error quaternion	t_i, t_{i-1}
<i>err_rr</i>	3	Satellite rate error	t_i, t_{i-1}
<i>a_rw</i>	3	Last executed reaction wheel action	t_{i-1}
<i>rwr</i>	3	Reaction wheel speeds	t_i, t_{i-1}
<i>mag_b</i>	3	Magnetic field vector	t_i, t_{i-1}
<i>err_rwr</i>	3	Reaction wheel speed error	t_i, t_{i-1}
<i>crm</i>	3	Cross product of <i>rwr</i> and <i>mag_b</i> scaled by 0.5	t_i
<i>bn</i>	1	Magnetic field norm	t_i

The reasoning behind this observation space design is that the agent is effectively given two consecutive system states as well as the last performed reaction wheel action, which allows it to calculate the dynamics of the system from the system state delta.

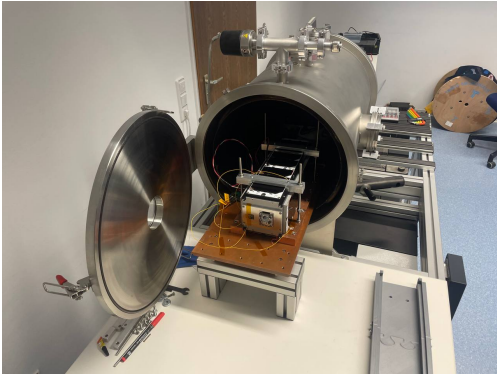
2.4. Calibration

To increase the fidelity of the simulation, available sensor data of the gyros and magnetometers was captured and used to augment the simulation and incorporated into the domain randomization during training. With the availability of telemetry data after the satellite’s launch, the moments of inertia could additionally be refined, and the residual magnetic dipole moments as well as the gyro bias determined. While the latter is generally part of regular mission operation, we applied machine learning techniques for refinement of the initial classical calibration.

2.4.1. Sensor Noise Model

To create the sensor noise model, measurement data from the gyroscopes (MEMS) and magnetometers (magneto-inductive) was recorded using the InnoCube EQM in a Thermal Vacuum (TV) chamber. The chamber was

evacuated to 10^{-4} mBar to eliminate convection effects and cooled. Figures 3a and 3b show the setup. Because the cooling units produce magnetic interference and vibration, data acquisition was performed only after reaching the target temperature with all pumps and cooling disabled. The EQM then warmed naturally back to approx. 30 °C room temperature, with the asymptotic temperature evolution compensated during data processing.



(a) InnoCube EQM in the Thermal Vacuum Chamber (open view).



(b) InnoCube EQM in the Thermal Vacuum Chamber (exterior view).

Figure 3: InnoCube EQM in the Thermal Vacuum Chamber (open and exterior views).

The dataset was cropped to match the in-orbit temperature range of -3.55 °C to 15.6 °C. In total, data from five experiments was evaluated and a sensor noise model was built. The noise model consists of a bias term v_b , sampled once per episode (corresponding roughly to an attitude maneuver) and white noise v_w (sampled every time step) during simulation.

The raw data was divided into 60 s segments (artificial “maneuvers”), assuming nearly constant bias within each segment. For each segment, the mean value was taken as the bias estimate. The standard deviation of the segment means forms σ_b . Since temperatures near room temperature are overrepresented, segment means were temperature-weighted based on their histogram distribution to avoid bias toward those ranges.

White noise statistics were obtained by subtracting each segment mean from the corresponding samples. The standard deviation of all residuals across all segments forms σ_n . For all simulations both σ_b and σ_n were additionally scaled by factor of 1.2 before the sampling step for domain randomization.

The noise sampling model can in brief be described by Equations (5)–(7):

$$v_b \sim \mathcal{N}(0, \sigma_b^2) \quad (5)$$

$$v_w \sim \mathcal{N}(0, \sigma_n^2) \quad (6)$$

$$v_{eff} = v_{sim} + v_b + v_w \quad (7)$$

The resulting parameters, derived exclusively from Thermal Vacuum Chamber conditions and without any temperature compensation applied, are given in Table 5.

Table 5: Sensor noise parameters used in simulation (after $1.2\times$ domain-randomization scaling). The values include the full uncompensated temperature-induced bias variations.

Axis	X	Y	Z
Gyroscopes			
Bias std σ_b ($^\circ/\text{s}$)	2.008×10^{-2}	1.419×10^{-2}	9.774×10^{-2}
White-noise std σ_n (rad/s)	1.381×10^{-2}	1.121×10^{-2}	1.056×10^{-2}
Magnetometers			
Bias std σ_b (μT)	5.477×10^{-2}	8.479×10^{-2}	7.578×10^{-2}
White-noise std σ_n (μT)	8.655×10^{-3}	9.074×10^{-3}	1.134×10^{-2}

These bias variations deliberately contain the complete uncompensated temperature drift over the full temperature cycle. This approximates the disturbance the AI agent is expected to encounter in orbit.

2.4.2. Moments of Inertia Estimation

Moments of inertia were determined via CAD, telemetry-based estimation, and analytical calculation. After cross-checking, the final values were set to $[0.0428, 0.0422, 0.00985]$ $kg\cdot m^2$. The maximum deviation from the CAD calculated values was approximately 2.5 %. For simulation, the moments of inertia were randomly varied by ± 15 % per axis and episode.

2.4.3. Residual Dipole Moment Estimation

During early operation of InnoCube, it was observed, that InnoCube exhibited unexpectedly high residual magnetic dipole moments. To refine the simulation model and with the early assumption, that momentum management has to be performed, the residual magnetic dipole moments were calculated using machine learning methods. Each MT axis provides approx. $0.35 Am^2$, which must (partially) compensate the residual dipole moments.

Residual dipole μ and gyro bias b were estimated from telemetry by solving a calibration problem based on Euler’s rotational dynamics [29]:

$$T_{\text{ext}} = I\dot{\omega} + \omega \times (I\omega) \quad (8)$$

$$T_{\mu} = \mu \times B \quad (9)$$

The optimization objective was:

$$\min_{\mu, b} \|I\dot{\omega} + \omega_{\text{corrected}} \times (I\omega_{\text{corrected}}) - \mu \times B\|^2 \quad (10)$$

where $\omega_{\text{corrected}} = \omega_{\text{measured}} + b$. The method was validated using simulated data with known ground truth and then applied to telemetry without actuator influence. Leveraging PyTorch [30] autograd gradient descent and the AdamW optimizer, we obtained:

$$\mu = [-0.459, -0.024, 0.069] \text{ Am}^2, \quad b = [-0.028, 0.761, -0.032] \text{ }^\circ/\text{s}.$$

Further validation was performed by activating MTs sequentially, obtaining the corresponding telemetry data and re-running the PyTorch script on this data. The resulting magnetic-field changes corresponded to dipole moments of 0.31–0.39 Am², which was in accordance with the expected theoretical values, thus confirming the magnetorquer characteristics and the correctness of the learned μ . The learned gyro bias was applied and replaced previous calibration for all gyro data processing of the InnoCube mission. For the training of the base-agent, the active residual dipole moment compensation was simulated with a random error of up to ± 10 % for each axis independently and up to ± 25 % for the flight-agent.

After applying the available dipole moment from one set of the magnetorquers, the in-orbit results showed a significant reduction of the residual dipole moment. To fully eliminate the residual in the x-axis, the second set of magnetorquers has to be used in the future, since the required dipole moment exceeds the available 0.35 Am² per single axis set. This, however is currently not implemented due to safety reasons, as this would require running both ADCS nodes simultaneously. In-orbit checks showed that the disturbance torque from the residual dipole moment decreased to an insignificant amount during an attitude maneuver, reducing the buildup of angular momentum, as reflected in smaller increases of the reaction-wheel speeds.

2.5. Base-Agent Training

Using our AI agent from [24] as a base, we derive the flight-agent through post-training, which is conceptually related to transfer learning. The base-agent is initially trained to solve the general attitude control problem. Subsequently, it undergoes post-training with modified boundary conditions and a revised optimization target to produce the flight-agent. This approach leverages the well-initialized policy that already captures the fundamental dynamics of the system, avoiding the need to re-learn this knowledge as compared to training the flight-agent from scratch. As outlined in Section 1 the flight-agent is based off of the RW subnetwork of the base-agent. In the following section, the base-agent training is described. The modifications performed to obtain the flight-agent are explained in Section 2.6.

2.5.1. Base-Agent Reward Functions

The base-agent was trained with a PPO derivative, SkipPPO [24], using separate subnetworks for RWs and MTs. The RWs learn to quickly attain the goal attitude, while the MTs learn slow RW momentum management to bring the RW speeds to ± 500 rpm (corresponding to ± 350 rpm and a safety buffer). The RW reward function of the base-agent rewards quick reduction of attitude error, reduction of angular rates, and stable convergence. The MT reward encourages minimizing RW speed deviations. A combined reward was used during post-training of the base-agent to balance both effects. The RW reward function is shown in Equations (11)–(16).

$$err_att_{t_i} = 1 - \delta q_{0,t_i} \quad (11)$$

$$\Delta\theta_{t_i} = err_att_{t_i} - err_att_{t_{i-1}} \quad (12)$$

$$p_norm_{t_i} = \|err_rr_{t_i}\| \quad (13)$$

$$p_att_{t_i} = 0.1 \cdot err_att_{t_i} \quad (14)$$

$$r_{t_i} = \begin{cases} 1 + \frac{1}{p_norm_{t_i} + 0.1}, & err_att_{t_i} < 3.8 \cdot 10^{-5} \\ e^{-err_att_{t_i}/0.14}, & err_att_{t_i} < err_att_{t_{i-1}} \\ 0.1 e^{-\Delta\theta_i/0.14} - 1, & \Delta\theta_{t_i} < \Delta\theta_{t_{i-1}} \\ e^{-err_att_{t_i}/0.14} - 2, & \text{else} \end{cases} \quad (15)$$

$$reward_rw_{t_i} = r_{t_i} - p_norm_{t_i} - p_att_{t_i} \quad (16)$$

δq_0 is the scalar component of the attitude error quaternion, p_norm penalizes satellite body rotation rates, and p_att penalizes residual attitude

error. It is to be noted, that if $\delta q_0 < 0$ then δq is multiplied by -1 prior to being passed to the AI agent. The main reward term r_{t_i} gives strong reward for achieving the target (within $\approx 1^\circ$), moderate reward for approaching it, slight penalties for overshooting correction and stronger penalties for diverging. The MT reward function is shown in Equations (17)–(19).

$$err_deviation_{t_i} = \sum err_rwr_{t_i} \cdot 16384.0 \quad (17)$$

$$p_action_{t_i} = \frac{\sum |a_mt_{t_i}|}{0.6 \cdot 50} \quad (18)$$

$$reward_mt_{t_i} = \frac{1 - p_action_{t_i}}{\sqrt{err_deviation_{t_i} + 1}} \quad (19)$$

Here, $a_mt_{t_i}$ are the current agent actions. The reward decreases with RW speed deviations and with MT action magnitude. It favors minimizing RW momentum with low dipole effort. For the base-agent post-training the reward function from Equation (20) was used.

$$reward_c_{t_i} = \frac{reward_rw_{t_i}}{11} + reward_mt_{t_i} \quad (20)$$

The RW reward is scaled to match MT reward magnitude to avoid bias. Table 6 shows the hyperparameters used, while Sections 2.5.2–2.5.5 describe the initial training and post-training process of the base-agent.

Table 6: Hyperparameters of the RW and MT subnetworks of the base-agent. Changes in parameters during base-agent post-training are only specified if they differ from the hyperparameters of the initial training.

Hyperparameter	RW Training/ Post-Training	MT Training/ Post-Training
total_timesteps	5×10^8	5×10^8
n_steps (rollout)	$2 \times 10^3 / 4 \times 10^4$	4×10^4
gamma	0.95	0.97 / 0.95
batch_size	64	64
clip_range	0.2	0.2
target_kl	0.2	0.2
learning_rate (init)	$1 \times 10^{-4} / 1 \times 10^{-5}$	5×10^{-5}
sde_sample_freq	1 per rollout	1 per rollout
log_std_init	-2.0	0.0 / -2.0
episode_length	50 / 5000	5000
num_skip	0	9 / 0

The networks were initialized using orthogonal weight initialization, with scaling factors of 0.01 for the RW action network, 10.0 for the MT action network, and 1.0 for all remaining networks. The RW policy and value networks consisted of three hidden layers of 64 neurons each for the policy and two hidden layers of 64 neurons each for the value network. The MT policy and value networks used four hidden layers of 64 neurons each for both policy and value components. All networks employed the SiLU activation function.

2.5.2. Subnetwork Policy

The base-agent employed a split policy network consisting of one RW subnetwork and one MT subnetwork, producing a six-element action vector by concatenating the three RW actions and the three MT actions. Each subnetwork can be in one of three states: DISABLED, FROZEN, or ACTIVE. DISABLED outputs zeros, does not contribute to training, and has non-trainable weights; FROZEN outputs effective actions but is not trainable; ACTIVE outputs effective actions and fully participates in training.

2.5.3. SkipPPO Trainer

The vastly different time horizons of the RWs and MTs, spanning two orders of magnitude, introduced a conflict in regards to the optimization targets and training hyperparameters. This introduced a pronounced credit assignment problem. The RWs have to focus on immediate rewards, as wrong RW commands can quickly spin up the satellite, while MTs have to consider long time horizons due to the small torques they generate. Further the MTs are underactuated and even single RW actions can cancel out hundreds of MT commands. Subsequently using the naive training approach it cannot always be determined which MT actions effectively contributed to a certain outcome and reward. To mitigate the credit assignment problem, PPO was modified to SkipPPO allow optional action freezing and effectively timestep skipping. When skip training is used, MT actions are frozen for num_skip steps while RW actions continue to be sampled each step. Rewards from skipped steps are accumulated and assigned to the initial MT action, mitigating the credit assignment problem and effectively shortening the MT episode length to $episode_length / (num_skip + 1)$.

2.5.4. *Initial Base-Agent Training*

Training consisted of initial base-agent training and base-agent post-training. For the initial training only orbit parameters and inertia variations were considered. The RW subnetwork was trained first with its reward and hyperparameters, attaining random target attitudes. Then, the RW network was frozen while the MT network was trained to reach RW speeds of ± 500 rpm. This sequential training resolved conflicts between actuator requirements and reward functions (short term focus vs long term focus).

2.5.5. *Base-Agent Post-Training*

For both subnetworks to adjust to each other, post-training has to be performed. The trainer receives both RW and MT configurations simultaneously and switches between both during post-training. This allows independent switching between RW- and MT subnetwork training within a single run, improving coordination without retraining from scratch. For stability, the joint reward function from Equation (20) was used. The optimization thus always accounted for both actuators. Since the basic attitude control behavior was already learned during the initial base-agent training, adaptation through post-training is simpler, and with neither subnetwork deactivated and the reward function unchanged, the value network can reliably predict expected future rewards without being reinitialized. For post-training therefore, the value network is carried over from the MT-training phase of the base-agent.

2.6. *Flight-Agent Training*

As mentioned in Sections 2 and 2.5, while initially designed for momentum management, the first in-orbit test was carried out using only the RW subnetwork, since the logic for operating the attitude controller outside of the pass windows was not yet implemented, thus making the momentum management part non viable due to the maneuver length being significantly longer than the pass duration (>2000 s). As the in-orbit tests used active magnetic residual dipole moment compensation using the MTs, we have decided to use the base-agent, trained as previously described, as starting point for finetuning, instead of training a new controller from scratch. The reasoning behind this was, that as the RW subnetwork of the base-agent had to learn to accommodate for disturbances introduced by the MTs, it would transfer to the disturbances from the active residual dipole moment compensation. The following sections describe the applied changes to the base-agent.

2.6.1. Safety Constraints

Shortly after deployment and prior to the first test, the safety limits were tightened (see 2.7.1. In particular the agents maximum rotation rates were limited to $20^\circ/\text{s}$ per axis. Further, the applied torque was constrained to 50 rpm/s per axis initially and and shortly after relaxed to 100 rpm/s . The maximum reaction wheel speeds were likewise initially set to $[1000, 1000, 500]\text{ rpm}$ and increased to $[1500, 1500, 700]\text{ rpm}$. These limitations were implemented via clipping. Nevertheless, we tested the base-agent, resulting in the first successful test of an AI-based attitude controller in orbit on October 30, 2025 during the pass from approximately 10:40 to 10:49 UTC. The initial attitude was $(-0.268, -0.851, -0.354, -0.280)$ with initial satellite body rates $(0.0227, -2.32, -1.74)^\circ/\text{s}$, and the goal attitude was $(1, 0, 0, 0)$. Figure 4 shows the Yaw, Pitch and Roll euler angles, the commanded RW torques, the RW speeds and the satellite body rates for the maneuver, together with the times of the attitude control command (new att. command) and when the goal attitude was attained with an error of $<1^\circ$ for all axes (steady-state start). All timestamps are given in UTC.

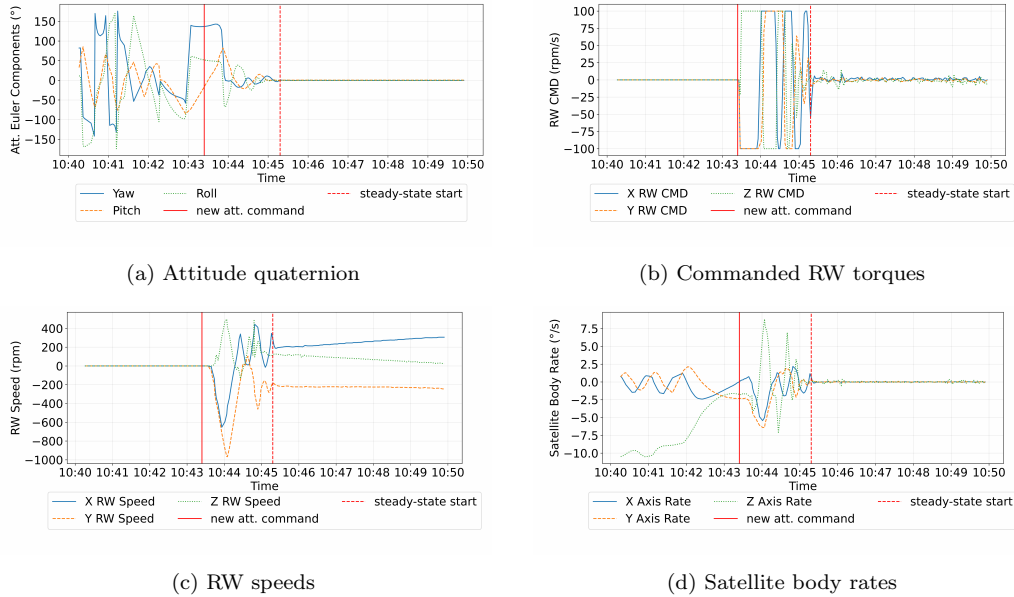


Figure 4: First in-orbit maneuver of the base-agent. Maneuver duration from attitude control command (new att. command) to achieving $<1^\circ$ error on all axes (steady-state start) on 2025-10-30: 10:43:24 to 10:45:18 (114 s). The maximum wheel speeds were limited to $[1000, 1000, 500]\text{ rpm}$ and the maximum torque to $[50, 50, 50]\text{ rpm/s}$ via clipping.

Figure 5 shows a detailed view of the steady-state period of the maneuver from Figure 4.

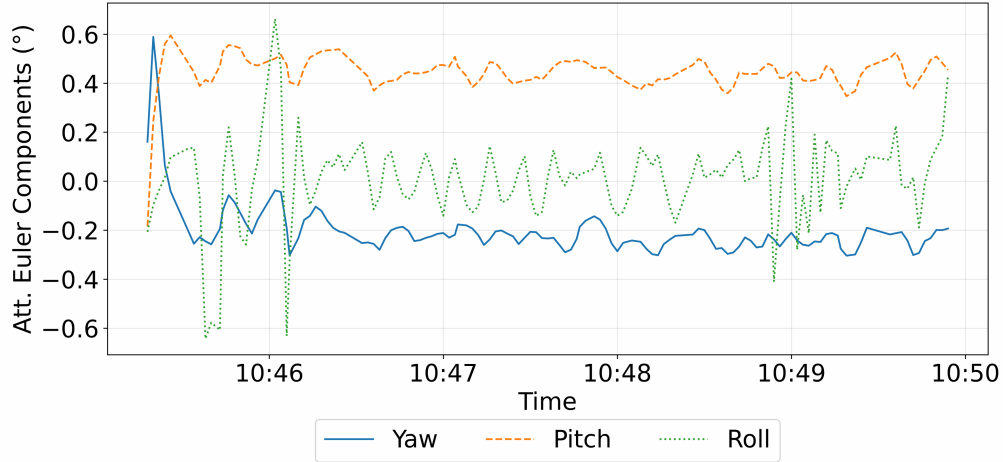


Figure 5: Steady-state section of the first in-orbit maneuver of the base-agent from Figure 4: Steady-state duration from 10:45:18 to 10:49:54 (276 s). The maximum wheel speeds were limited to [1000, 1000, 500] rpm and the maximum torque to [50, 50, 50] rpm/s via clipping.

Table 7 shows the numeric values for the minimum, maximum, mean and standard deviation of the yaw, pitch and roll angles for the steady-state period. The start of the steady-state period is defined as the earliest time at which the attitude deviations across all three axes remain below 1° for a continuous duration of at least 15 seconds. It is to be noted, that these values have to be interpreted qualitatively since they include existing measurement noise and potential remaining gyro bias, which is difficult to determine exactly without an external reference. All values are based on raw telemetry data. The telemetry data was captured at a sampling frequency of 0.5 Hz, exported from the InnoCube mission's Grafana dashboard, and is available in the GitHub repository at <https://github.com/kdjebko/lelar-in-orbit-data>.

Table 7: Roll, Pitch, Yaw Error - Steady-state error statistics for the maneuver shown in Figure 4 on 2025-10-30 from 10:45:18 to 10:49:54 (276 s) in degrees.

Component	Min	Max	Mean	Std
Yaw	-0.30	0.59	-0.20	0.11
Pitch	-0.18	0.59	0.44	0.08
Roll	-0.64	0.66	0.00	0.18

The RW subnetwork of the base-agent could operate under the clipping, although it was not part of the training, and was only (indirectly) affected by the 20 °/s per axis limit. Exceeding this rate results in an instant shutdown of the controller. Since the base-agent was trained without a rotation rate constraint, the agent may exceed this limit when trying to attain distant attitudes. We decided to perform a post-training run for the base-agent considering these constraints for a fair performance evaluation. Table 8 lists the relevant introduced safety-constraints and the appropriate settings for the base-agent training.

Table 8: Parameter constraints for base-agent training and Safety Cage limits.

Parameter	Base-Agent Training	Safety Cage Limits
Max RW Speed	$[1.64, 1.64, 1.64] \times 10^4$ rpm	$[1.5, 1.5, 0.7] \times 10^3$ rpm
Max RW Torque	$[336.24, 336.24, 336.24]$ rpm/s ($[2.0, 2.0, 2.0] \times 10^{-3}$ Nm)	$[100, 100, 100]$ rpm/s
Max Satellite Rotation Rate	no limit imposed	$[20, 20, 20]$ °/s

Additionally, the RW min torque was marginally corrected to $[1.5, 1.5, 1.5] \times 10^{-5}$ Nm after a cross-check with InnoCube. The flight-agent training was adjusted by changing the initial RW speeds from ± 500 rpm to 0 rpm per axis to reflect the standalone nature of the RW subnetwork. Further, the simulated boundary condition variations were increased for improved robustness and to make efficient use of the post-training run. The residual magnetic dipole moment compensation error was raised from ± 10 % to ± 25 % per axis and the initial satellite body rates were varied in the interval $[-5, 5]$ °/s per axis. Table 9 lists the modifications to the simulation scenario applied during the training of the flight-agent.

Table 9: Simulation environment adjustments performed for the flight-agent.

Parameter	Base-Agent Training	Flight-Agent Training
Init RW Speeds	± 500 rpm per axis	0 rpm per axis
Initial Satellite Body Rates	0 $^\circ$ /s per axis	sampled from $[-5, 5]$ $^\circ$ /s per axis
Residual Magnetic Dipole Compensation Error	± 10 % per axis	± 25 % per axis

2.6.2. Flight-Agent Reward Function and Post-Training

Based on the changed requirements regarding the satellite body rates, a modified reward function was employed. The Safety Cage limits from Table 9 were incorporated into the simulation. While they were not negatively affecting the agents performance in particular, they have been included here since it was not associated with further training cost. The modified reward function for the RW subnetwork is shown in Equations (21)–(29).

$$err_att_{t_i} = 1 - \delta q_{0,t} \quad (21)$$

$$\Delta\theta_{t_i} = err_att_{t_i} - err_att_{t_{i-1}} \quad (22)$$

$$p_norm_{t_i} = \|err_rate_{t_i}\| \quad (23)$$

$$p_att_{t_i} = 0.1 \cdot err_att_{t_i} \quad (24)$$

$$p_rates_excess_{t_i} = \sum_{k=1}^3 c \cdot (\max(0, |err_rate_{t_i}[k]| - \text{threshold}))^2 \quad (25)$$

$$p_smooth_{t_i} = k_{smooth} \|a_{t_i} - a_{t_{i-1}}\|^2 \quad (26)$$

$$p_rates_{t_i} = 0.5 \cdot p_norm_{t_i}^2 \quad (27)$$

$$r_{t_i} = \begin{cases} 1 + \frac{1}{p_norm_{t_i} + 0.1} + \frac{1}{err_att_{t_i} \cdot 10^5 + 0.1}, & \text{if } err_att_{t_i} < 3.8 \cdot 10^{-5} \\ e^{-\frac{err_att_{t_i}}{0.14}}, & \text{elif } err_att_{t_i} < err_att_{t_{i-1}} \\ 0.1 \cdot e^{-\frac{\Delta\theta_{t_i}}{0.14}}, & \text{elif } \Delta\theta_{t_i} < \Delta\theta_{t_{i-1}} \\ e^{-\frac{err_att_{t_i}}{0.14}} - 1, & \text{else} \end{cases} \quad (28)$$

$$reward_rw_{t_i} = r_{t_i} - p_att_{t_i} - p_rates_excess_{t_i} - p_smooth_{t_i} - p_rates_{t_i} \quad (29)$$

The main change compared to the RW reward function of the base-agent was the increase of the rotation rate regularization and the inclusion of the penalty terms $p_rates_excess_{t_i}$ to punish rotation rates exceeding a certain threshold and $p_smooth_{t_i}$ to penalize bang-bang behavior to avoid reward hacking in conjunction with the rotation rate penalty. The parameter *threshold* was set to 10.0 (°/s; as soft maximum for the desired satellite body rates, recommended by InnoCube operators, to provide a buffer to the Safety Cage limit of 20°/s per axis) and the parameter *c* to 5.0. Further, the first term of r_{t_i} was augmented to reward the agent stronger for lower steady state errors. For the fine tuning through post-training, the RW hyperparameters (post-training) from Table 6 were used but with *n_steps* set to 2×10^3 , episode length set to 100 and the total timesteps doubled to 1×10^9 .

2.7. Safety Cage and Integration

Two new modules were introduced to the InnoCube’s ADCS software, which are necessary for the LeLaR execution on-board: a Safety Cage module, which ensures safe execution of control experiments, and the LeLaR controller module, which implements the developed AI agent.

2.7.1. Safety Cage

In order to assure that mission critical states resulting from unwanted controller behaviour are not reached during attitude control maneuvers, a Safety Cage architecture as proposed in [31] is implemented. This construct, recommended by the ECSS Machine Learning Handbook, uses a set of rules, to prevent the system from entering potentially dangerous states. This can be achieved through a set of safety interventions, which will be activated once a certain rule is triggered. Potentially critical failure modes for the InnoCube satellite have been identified using the proposed Failure Mode, Effects and Criticality analysis (FMECA). This analysis led to the following main critical failure modes:

- High rotational body rates during a maneuver
- High rotational body rates after a maneuver
- Magnetorquer induced high rotational body rates
- Blind spot orientation of main antenna
- Uploaded network files causing software errors

The available angular momentum from the reaction wheels could potentially result in very high satellite body rates (exceeding $20^\circ/\text{s}$) in case of a malfunctioning control law. High satellite body rates pose different risks to the mission. The four flexible antenna-rods extending out of the structure could bend under the resulting torques, potentially deforming the antenna pattern or even causing damage. High rotational rates might also limit the capability of receiving and transmitting messages using the transmitter system and limit the capability to perform appropriate maximum power-point tracking for the solar panels. Through the buildup of disturbance angular momentum resulting from external disturbance torques, high rotational body rates might be induced when powering-off reaction-wheels, which have not been desaturated. In case of a power-failure or system malfunction, high rotational rates may be induced, which leads to the same problems as mentioned before. Incorrect commanded magnetorquer outputs might also lead to high rotational body rates, especially if applied for a prolonged period of time. Since InnoCube is using a circular-polarized antenna paired with a circular-polarized antenna on ground, certain orientations exist which put the satellite in a blind-spot orientation, where transmission and reception of telemetry or telecommands becomes unavailable. If such an orientation is reached during a control maneuver, the satellite becomes unreachable, which poses a high operational risk.

Neural network weights can be uploaded to the satellite as files. Since loading these network files poses the possibility of a software crash (e.g., due to misconfigured parameters or software bugs), particular focus needs to be placed on the safe loading of these files. The latter prevented by not allowing uploaded network files to be loaded automatically into the controller module. This ensures that corrupted files do not compromise the safe booting of the ADCS software, as the module can be reset externally via PCDU commands. While ground testing using InnoCube's engineering qualification model (EQM) is being done for new network files (or software updates), the same principle applies to satellite missions in general.

To mitigate the risk of reaching unsafe states during ADCS control experiments, a Safety Cage architecture is integrated into the existing ADCS software. The Safety Cage augments the existing FDIR schemes by adding two components: a monitoring module, that observes specific telemetry parameters and triggers in case of violation of safety rules, and software defined hard limits on actuator or procedural parameters. The main parameters, which include hard software limits, are reaction wheel torque and maximum

speed. Limiting these (in particular the maximum reaction wheel speeds), restricts the maximum satellite body rates which can be achieved during an experiment. Operators can select limits to ensure safe operation, even if all reaction wheels are saturated. The same is true for the maximum stored angular momentum from the reaction wheels after an experiment, which could spin up the satellite in case the reaction wheels are turned off without using proper desaturation using the magnetorquers. During LeLaR experiments, limiting the maximum reaction wheel speed has been the main Safety Cage parameter, as it posed the highest risk of uncontrolled satellite tumbling.

The monitoring module runs in parallel and independently from the control loop. It receives all ADCS telemetry (e.g., raw sensor data, sensor and actuator states, and possible anomalies) and compares them against telecommanded rules. The underlying rationale is that software bugs, operator errors, or other unforeseen problems might still cause the system to enter critical states, even when hard rules are in place. The monitored parameters are those, which have already been defined as hard software limits (e.g., reaction wheel speeds) as well as other telemetry data, such as satellite rotational rates.

Exceeding a predefined limit causes the ADCS to disable the active controller and enter an idle state, where no actuator commands are being issued. After a set period, the reaction wheels are turned off to conserve power. While it is possible to automatically switch to active detumbling using the magnetorquers, this was deemed unnecessary given the maximum rotational rates observed during experiments. Since InnoCube's energy budget is power-positive while tumbling (since the solar-panels are mounted on each long side of the satellite), being in an idle state with deactivated actuators is both safe and efficient. After a safety trigger, it is the operator's responsibility to reset and reconfigure the system for new experiments. Blind spot orientations of the main antenna proved not to be a major practical concern, as the link-margin exceeded expectations and those orientations could be avoided by manually commanding new attitudes.

The main Safety Cage constraints used during the in-orbit experiments are described in section 2.6.1. It is worth noting that the Safety Cage architecture can be seen independently from the AI-controller, because it treats the system as a black-box and uses mainly external observable telemetry to ensure safe operation. The same techniques are therefore applicable to classical controllers and are effectively, to some extent, part of traditional FDIR techniques.

2.7.2. InnoCube LeLaR Integration

Due to the the modular ADCS software design, integrating the LeLaR controller module into the existing software is straight forward. The controller module treats the control law implementation as an input-output black-box, as depicted in Figure 2. It accepts the current attitude, satellite body rates, and current sensor values, and outputs a control torque request to the actuators. Figure 6 schematically shows the LeLaR Controller Module implementation. Internally, the module is divided into two main components: the network inference engine and the network loader. The network inference engine runs the forward pass of the neural network given a set of input values (the observation vector) and produces a set of output values (the actuator actions). The inference is based on a bare-metal implementation of a fully connected, Multi-Layer Perceptron (MLP) neural network. Without special emphasis on code optimization, the inference engine can execute a full forward pass in approximately 38 ms, which is sufficiently fast considering the 1 Hz control loop frequency.

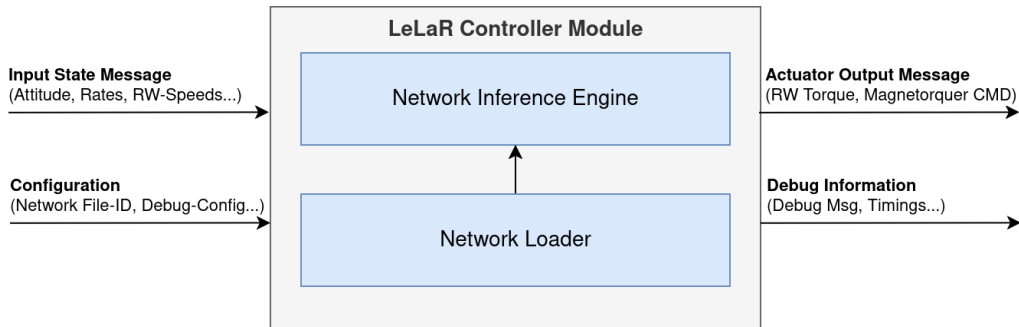


Figure 6: LeLaR Controller Module.

The network loader allows changing the loaded network by reading network parameters from a file stored on the ADCS mainboard. A network parameter file contains information about the network layer structure as well as the set of weights and bias values which have been derived during training of the AI agent on ground. For the flight-agent, the fully trained and uncompressed network file resulted in a binary file of approximately 105 kB in size. Multiple network files can be stored on-board and loaded as needed using telecommands, allowing different trained networks to be evaluated efficiently during in-orbit experiments.

3. Results

In the following, first the discrepancies between the simulated and the real-world behavior of the physical satellite are discussed and then the results from different in-orbit maneuvers of the AI-based attitude controller are presented. Two types of inertial pointing maneuvers were considered. The first type corresponds to the initial maneuver after activating the AI-based attitude controller and features a random initial attitude, i.e., the attitude at the time the experiment starts. For subsequent maneuvers, corresponding to the second type, the current attitude was set to a specified value. For all maneuvers, the goal attitude was commanded to be $(1, 0, 0, 0)$. This choice is equivalent to maintaining the current attitude or commanding specific goal attitudes, but it enabled quick visual comparability during ground passes based on the attitude quaternions from the raw housekeeping telemetry data available via the InnoCube mission’s Grafana dashboard.

3.1. *Sim2Real discrepancies*

The actual satellite behavior diverged from the simulation setup of the flight-agent. The reaction wheels showed a few peculiarities, which were not accounted for during training and which we demonstrate in Section 3.2.1. The reaction wheels exhibit reduced reliability in the range of $[-350, 350]$ rpm. The measured wheel speeds can show sudden jumps by more than 150 rpm, creating a discrepancy between the measured and executed wheel speeds. Another issue is, that when turning the reaction wheels on at the experiment start, each wheel has a random dead time of up to approximately 20 seconds. It can happen, that e.g., the X-RW starts spinning immediately, while the Y- and Z-RW only start responding 20 seconds later. While this behavior was also not modeled in simulation, this too posed no observable issues for the AI agent. Additionally, it was expected to employ both sets of magnetorquers for residual dipole moment compensation. This compensation was assumed and modeled in simulation. However the planned software update to enable simultaneous operation of both ADCS modules was scrapped due to safety reasons and hence only one set of magnetorquers remained for active dipole moment compensation. While it would have been possible to collect data and then adjust the simulation model of the RWs, we decided against it to show the ability of the AI agent to adapt to deviations from the expected boundary conditions. Regarding the residual dipole moment compensation, also no further adjustment to the simulation was made, as the simulated

compensation error window of 25 % was large enough to include the single MT case. Generally, it is neither always possible nor is it intended to perform adjustments to the simulation after deployment. These discrepancies have to be compensated by the AI-based controller out-of-the-box. Hence the only reason to refine the simulation at this point is to investigate the maximal achievable performance, which is not the intention of this work.

3.2. In-Orbit Results

In the following, we present the in-orbit experiments conducted with the InnoCube nanosatellite. We first demonstrate the effect of the reaction wheels becoming trapped within a narrow rotation speed interval and illustrate a representative inertial pointing maneuver in the presence of RW dead time. Subsequently, we discuss two sets of experiments comparing the AI-based attitude controller with the classical PD controller currently implemented onboard InnoCube. The first experiment consists of repeated executions of an identical rotational maneuver, while the second experiment evaluates the tracking performance for a predefined sequence of attitudes. The maneuver telemetry data (including the Data of the first base-agent maneuver from Figure 4a) was captured at a sampling frequency of 0.5 Hz and is available in the GitHub repository at <https://github.com/kdjebko/lelar-in-orbit-data> as obtained via export from the InnoCube mission’s Grafana dashboard.

The experimental results are assessed using steady-state performance metrics. This choice is motivated by the limited observability and repeatability of transient dynamics in the in-orbit environment, which are strongly influenced by unmodeled disturbances, actuator nonlinearities, and timing uncertainties, especially given the limited number of experiments that can be performed in-orbit. In contrast, steady-state behavior provides a robust and comparable measure of control performance, directly reflecting pointing accuracy and enabling a meaningful comparison between controllers in the presence of the aforementioned deviations and disturbances.

3.2.1. In-Orbit RW Behavior

The RWs exhibited certain behavioral characteristics impeding attitude control when being operated in low rpm ranges. This includes sudden jumps of the measured RW speeds, unresponsiveness to RW commands near 0 rpm and a random dead time after turning the RWs on. Figure 7 shows in-orbit data of an RW test from December 15, 2025. A sudden jump in the measured

RW speeds by approximately 185 rpm is present at 21:48:54. As can be seen by the unaffected satellite attitude, this outlier is purely a measurement artifact.

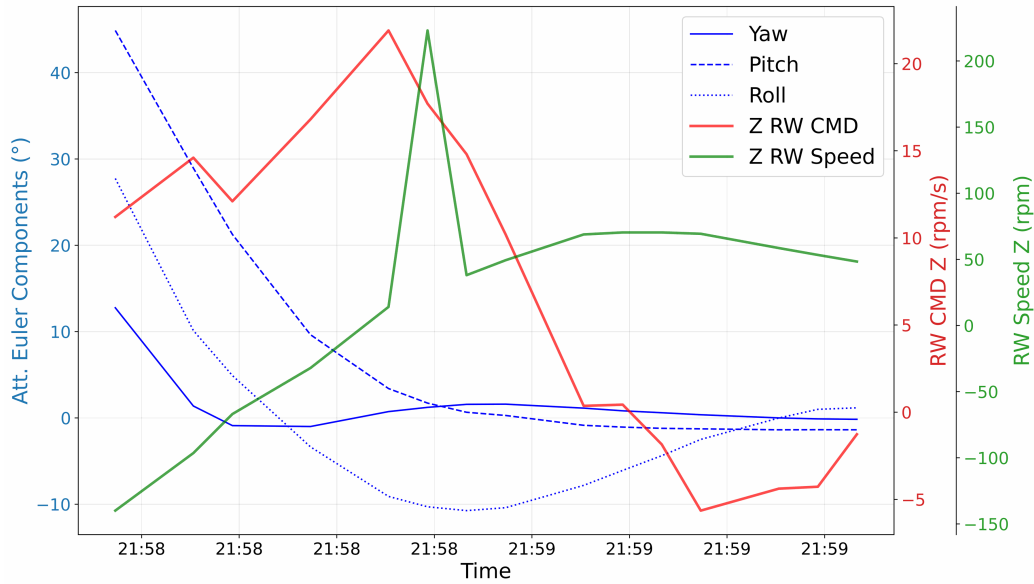


Figure 7: In-Orbit data showing a sudden jump of measured RW speed.

Figure 8 shows rate estimator inaccuracies and unresponsiveness of the RWs near zero from December 08, 2025. Around 20:23:20 and 22:23:38 the AI agent commands positive torques for the X-RW, which does not react for several seconds, and then suddenly spikes. This happens twice in a row and is responsible for delayed attainment of the steady-state.

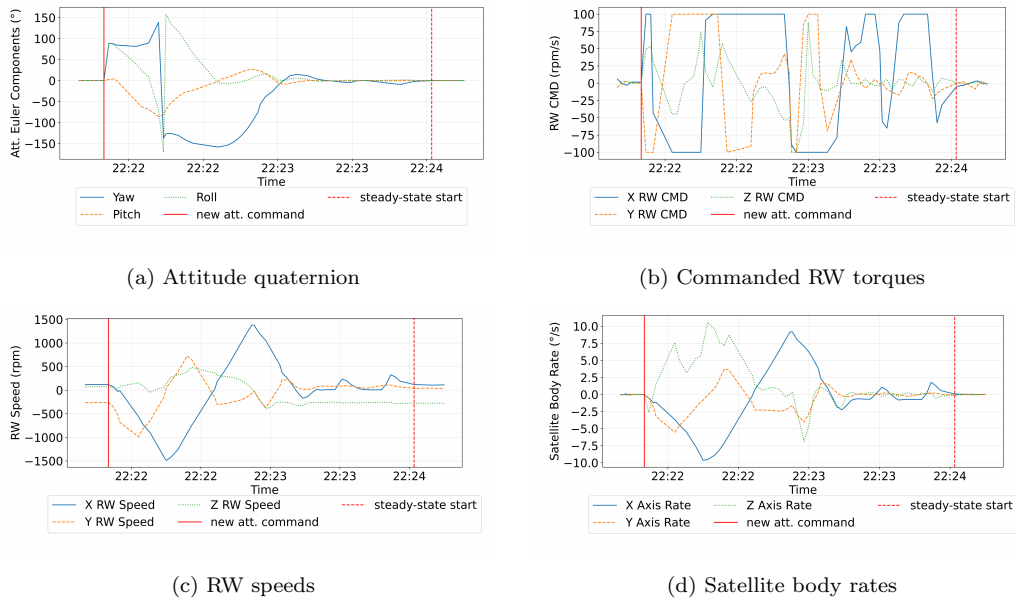


Figure 8: Attitude determination and control performance during the maneuver on 2025-12-08 from 22:21:50 (commanded attitude) to 22:24:02 (steady-state start)

Figure 9 shows a detailed snapshot of this timeframe. It can be seen, that the X-RW does not respond to commanded torques, making it impossible to accurately maintain the goal attitude. On the other hand side, the AI agent maintains control during these periods and attains the steady-state reliably as soon as the RWs resume operation.

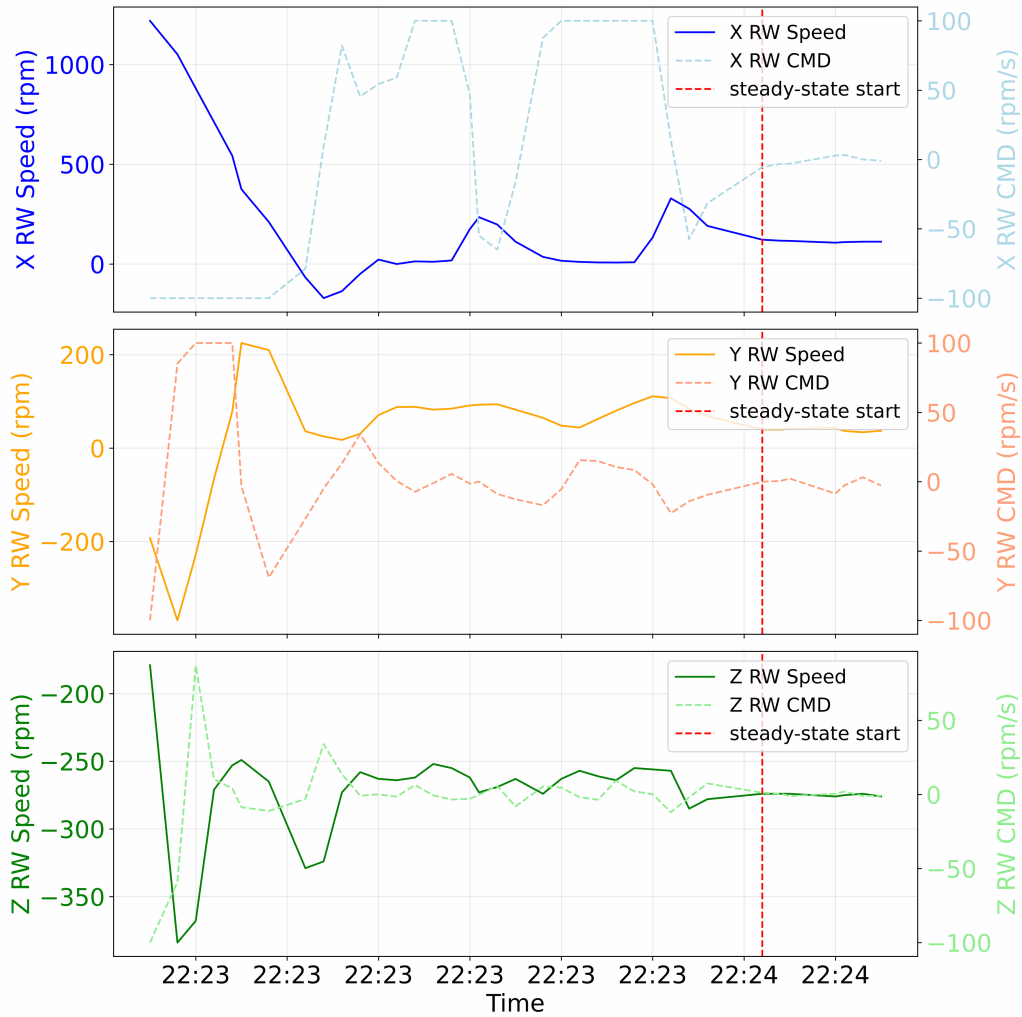


Figure 9: Snapshot from the maneuver of Figure 8, illustrating the unresponsiveness of the X-RW towards commanded torques.

Another issue encountered was that the RWs have a dead time for a random amount of time up to approximately 20 s after being first turned on. During this time the RWs are unresponsive to commanded torques. Figure 10 shows an example maneuver from December 13, 2025 including RW dead time. For this maneuver, at the time of commanding the goal attitude (1, 0, 0, 0), the initial attitude was (-0.530, -0.0994, -0.418, 0.732) with initial rotation rates (-0.140, -0.137, 6.16) °/s.

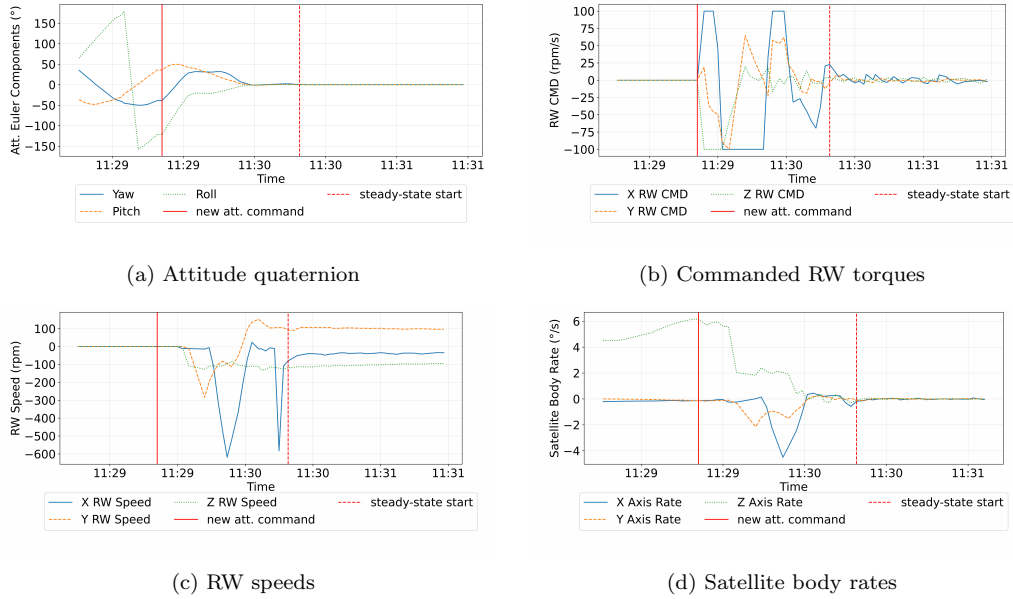


Figure 10: Attitude maneuver from 2025-12-13 with duration from commanded attitude to steady-state start: 11:29:21 to 11:30:19 (58.0 s).

It can be seen from Figure 10 (c), that the reaction wheels do not react immediately, instead the Z-RW reacts first, followed by the Y-RW and finally the X-RW after a random delay that cannot be anticipated in advance. Table 10 quantifies the steady-state period. As with Table 7 the start of the steady-state period is defined as the time where the attitude deviations of all three axes settle below 1° each for at least 15 seconds.

Table 10: Roll, Pitch, Yaw Error - Steady-state error statistics for maneuver from 2025-12-13 11:30:19 to 2025-12-13 11:31:28 (69 s) in degrees.

Component	Min	Max	Mean	Std
Yaw	-0.12	0.38	0.03	0.09
Pitch	-0.08	0.33	0.04	0.07
Roll	-0.30	0.04	-0.09	0.07

Figure 11 visualizes the steady-state-period of the maneuver from Figure 10.

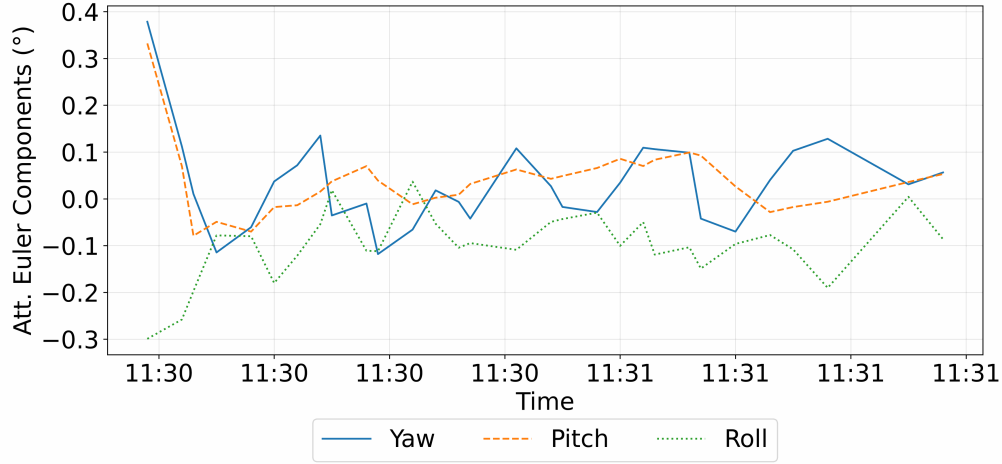


Figure 11: Steady-state section of a maneuver of the flight-agent from Figure 10. Steady-state period: 11:30:19 to 11:31:28 (69 s).

3.2.2. Comparison with the PD Controller for Repeated Maneuvers

Experiments using command lists were performed where a rotation from $(-0.5, -0.5, -0.5, -0.5)$ to $(1, 0, 0, 0)$ was conducted repeatedly. For the first maneuver, the current attitude and satellite body rates were unmodified and the goal attitude was set to $(1, 0, 0, 0)$. For all subsequent maneuvers, the procedure was to set the current attitude to $(-0.5, -0.5, -0.5, -0.5)$ and then to command $(1, 0, 0, 0)$ as goal attitude. For these maneuvers, the initial rates were close to 0. A delay of 120 s between maneuvers was used allowing for seven maneuvers to be completed in the maximum experiment timeframe of 15 minutes, which was set due to safety and power constraints for unsupervised experiments. Figures 12–15 show the attitude quaternions, commanded RW torques, RW speeds and satellite body rates, along with the maneuver start and settling-time start times for a LeLaR flight-agent experiment from December 17, 2025. The initial attitude for the first maneuver was $(0.973, -0.0967, 0.105, -0.180)$ and the initial satellite body rates were $(-0.974, 0.917, -1.46)$ °/s.

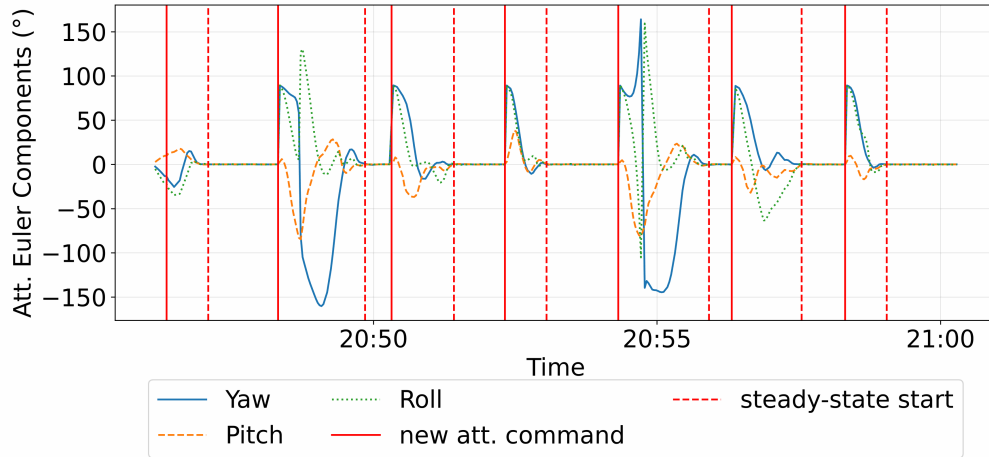


Figure 12: Attitude quaternion for seven LeLaR flight-agent maneuvers from commanded attitude to steady-state start on 2025-12-17. Maneuver 1: 20:46:21–20:47:05 (44 s), Maneuver 2: 20:48:19–20:49:51 (92 s), Maneuver 3: 20:50:19–20:51:25 (66 s), Maneuver 4: 20:52:19–20:53:03 (44 s), Maneuver 5: 20:54:19–20:55:55 (96 s), Maneuver 6: 20:56:19–20:57:33 (74 s), Maneuver 7: 20:58:19–20:59:03 (44 s).

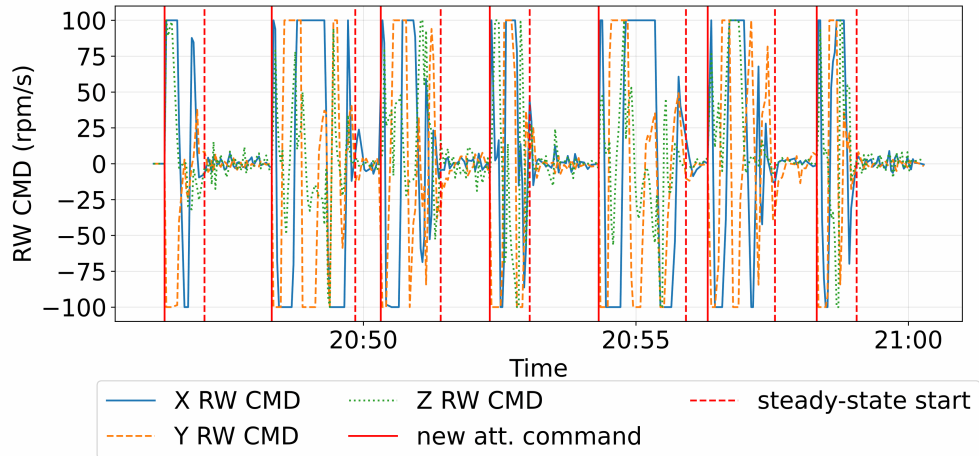


Figure 13: Commanded reaction wheel torques during seven LeLaR maneuvers from commanded attitude to steady-state start on 2025-12-17. For the timestamps see Figure 12.

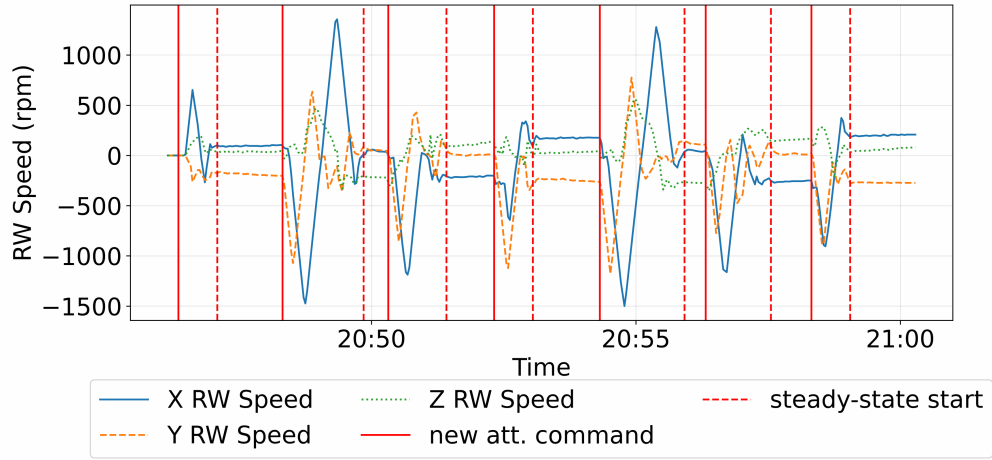


Figure 14: Reaction wheel speeds during seven LeLaR maneuvers from commanded attitude to steady-state start on 2025-12-17. For the timestamps see Figure 12.

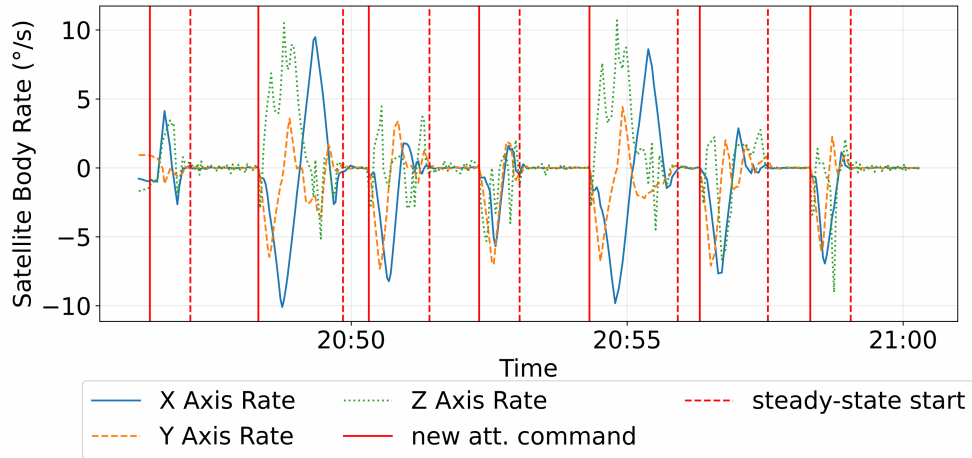


Figure 15: Satellite body rates during seven LeLaR maneuvers from commanded attitude to steady-state start on 2025-12-17. For the timestamps see Figure 12.

The tables 11–17 quantify the steady-state behavior of the maneuvers.

Table 11: Yaw, Pitch, Roll Error - Maneuver 1: Steady-state error statistics from 2025-12-17 20:47:05 to 2025-12-17 20:48:19 (74 s) in degrees.

Component	Min	Max	Mean	Std
Yaw	-0.06	0.11	0.03	0.04
Pitch	-0.06	0.18	0.11	0.05
Roll	-0.43	0.43	0.03	0.20

Table 12: Yaw, Pitch, Roll Error - Maneuver 2: Steady-state error statistics from 2025-12-17 20:49:51 to 2025-12-17 20:50:19 (28 s) in degrees.

Component	Min	Max	Mean	Std
Yaw	-0.52	0.74	0.04	0.30
Pitch	-0.47	0.17	-0.00	0.18
Roll	-0.35	0.14	-0.02	0.15

Table 13: Yaw, Pitch, Roll Error - Maneuver 3: Steady-state error statistics from 2025-12-17 20:51:25 to 2025-12-17 20:52:19 (54 s) in degrees.

Component	Min	Max	Mean	Std
Yaw	-0.04	0.29	0.08	0.09
Pitch	-0.13	0.48	0.12	0.19
Roll	-0.51	0.63	-0.04	0.30

Table 14: Yaw, Pitch, Roll Error - Maneuver 4: Steady-state error statistics from 2025-12-17 20:53:03 to 2025-12-17 20:54:19 (76 s) in degrees.

Component	Min	Max	Mean	Std
Yaw	-0.39	0.11	0.02	0.09
Pitch	-0.28	0.89	0.13	0.17
Roll	-0.91	0.63	-0.04	0.32

Table 15: Yaw, Pitch, Roll Error - Maneuver 5: Steady-state error statistics from 2025-12-17 20:55:55 to 2025-12-17 20:56:19 (24 s) in degrees.

Component	Min	Max	Mean	Std
Yaw	-0.47	0.15	-0.05	0.22
Pitch	-0.05	0.30	0.13	0.11
Roll	-0.18	0.22	-0.01	0.12

Table 16: Yaw, Pitch, Roll Error - Maneuver 6: Steady-state error statistics from 2025-12-17 20:57:33 to 2025-12-17 20:58:19 (46 s) in degrees.

Component	Min	Max	Mean	Std
Yaw	-0.05	0.41	0.05	0.12
Pitch	-0.31	0.50	0.07	0.25
Roll	-0.18	0.18	-0.06	0.09

Table 17: Yaw, Pitch, Roll Error - Maneuver 7: Steady-state error statistics from 2025-12-17 20:59:03 to 2025-12-17 21:00:17 (74 s) in degrees.

Component	Min	Max	Mean	Std
Yaw	-0.07	0.17	0.04	0.05
Pitch	-0.04	0.14	0.03	0.04
Roll	-0.42	0.27	-0.12	0.16

The same experiment was conducted using the original PD controller of InnoCube. The PD controller serves as the original InnoCube controller and was manually tuned in simulation, independently of the LeLaR AI agent training. It is worth noting that the original PD controller had not been optimized to the fullest extent and only served as a suitable controller for InnoCube’s original requirements. Therefore, this analysis currently does not serve as a comparison of the maximal possible performance between a PD controller and the LeLaR controller since both controllers were designed using different optimization requirements. However, the original PD controller allows for a preliminary qualitative comparison between a classical controller and our AI-based controller in a similar execution environment. An analysis of the maximal performance of both controllers after specialization is subject to future work. Again, the same seven maneuvers were commanded as for the LeLaR flight-agent. Each time the initial attitude was set to (-0.5, -0.5,

(-0.5, -0.5) and the goal attitude to (1, 0, 0, 0). Given a goal steady-state requirement of 1° for each axis, the goal steady-state was only attained during the maneuvers 3, 5, and 6. For the first maneuver, the initial attitude was (0.893, -0.0282, -0.0269, 0.448) and the initial satellite body rates were (-0.348, -0.244, 4.09) $^\circ/s$. Figures 16–19 visualize the PD maneuvers from the experiment conducted on December 15, 2025.

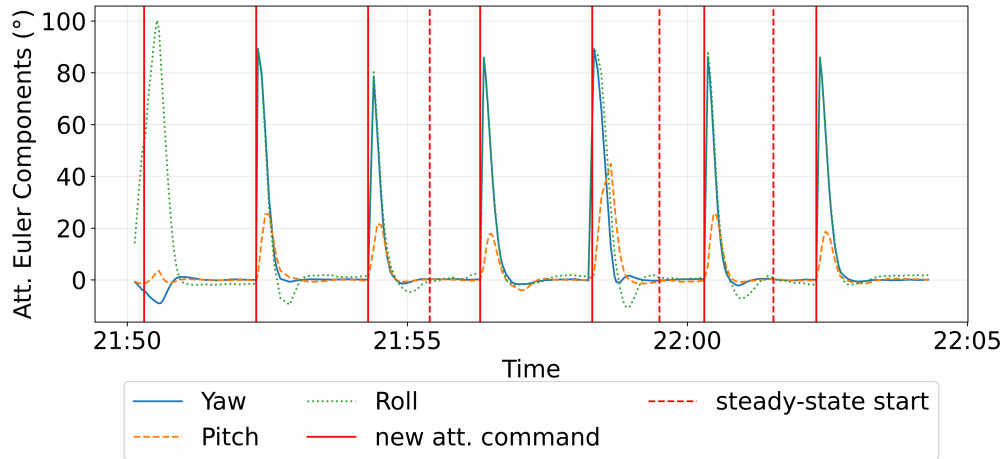


Figure 16: Attitude quaternion for seven PD maneuvers from commanded attitude to steady-state start on 2025-12-15. Given a goal steady-state limit of 1° for each axis, the goal steady-state was only attained during three maneuvers from 21:54:18 to 21:55:24 (Maneuver 3; 66 s), from 21:58:18 to 21:59:30 (Maneuver 5; 72 s) and from 22:00:18 to 22:01:32 (Maneuver 6; 74 s). The other maneuver start times were: Maneuver 1 - 21:50:18, Maneuver 2 - 21:52:18, Maneuver 4 - 21:56:18, Maneuver 7 - 22:02:18.

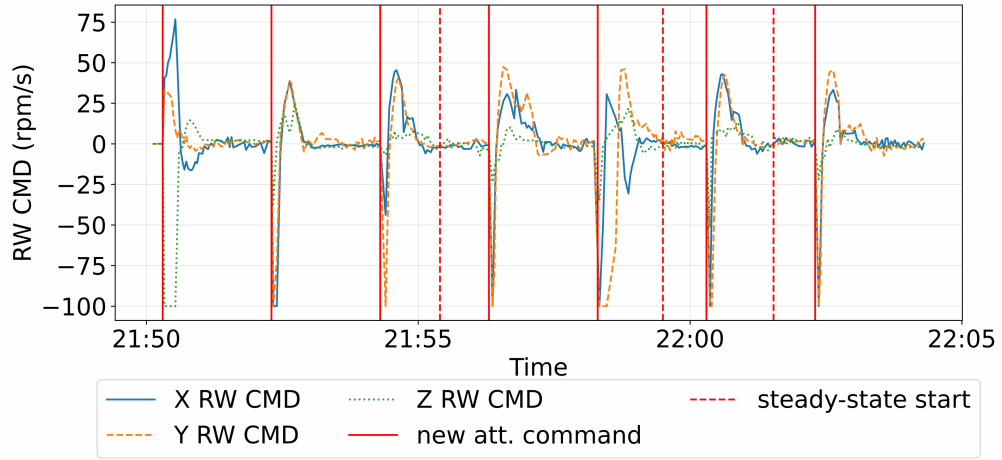


Figure 17: Commanded reaction wheel torques during seven PD maneuvers from commanded attitude to steady-state start on 2025-12-15. For the timestamps see Figure 16.

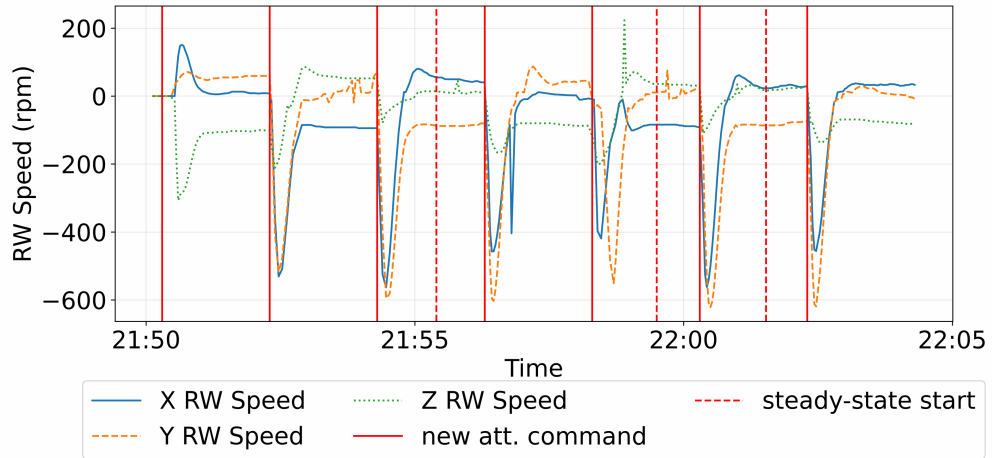


Figure 18: Reaction wheel speeds during seven PD maneuvers from commanded attitude to steady-state start on 2025-12-15. For the timestamps see Figure 16.

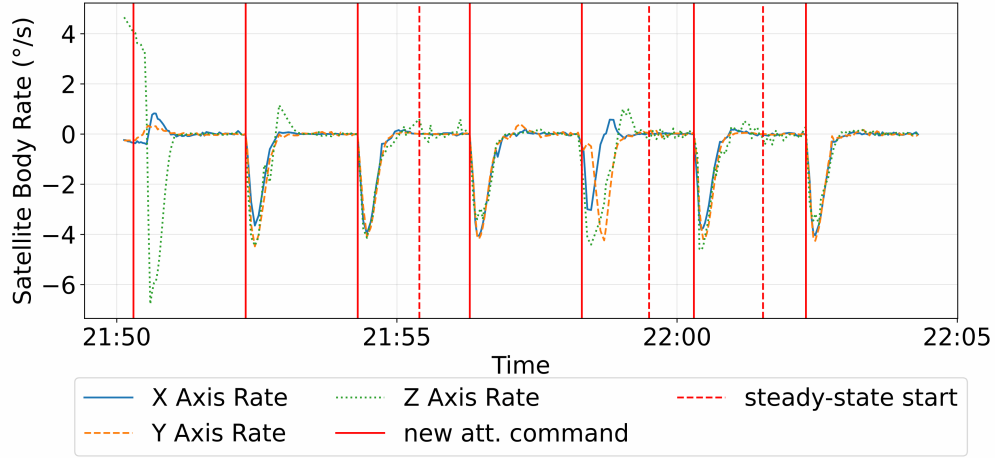


Figure 19: Satellite body rates during seven PD maneuvers from commanded attitude to steady-state start on 2025-12-15. For the timestamps see Figure 16.

Tables 18–20 shows the steady-state statistics for the successful PD maneuvers 3, 5, and 6.

Table 18: Yaw, Pitch, Roll Error - Maneuver 3: Steady-state error statistics from 2025-12-15 21:55:24 to 2025-12-15 21:56:18 (54 s) in degrees.

Component	Min	Max	Mean	Std
Yaw	-0.01	0.34	0.22	0.10
Pitch	-0.33	0.23	-0.00	0.20
Roll	-0.43	2.58	0.75	0.92

Table 19: Yaw, Pitch, Roll Error - Maneuver 5: Steady-state error statistics from 2025-12-15 21:59:30 to 2025-12-15 22:00:18 (48 s) in degrees.

Component	Min	Max	Mean	Std
Yaw	-0.23	0.32	0.12	0.18
Pitch	-0.75	-0.22	-0.50	0.17
Roll	0.18	0.99	0.54	0.23

Table 20: Yaw, Pitch, Roll Error - Maneuver 6: Steady-state error statistics from 2025-12-15 22:01:32 to 2025-12-15 22:02:18 (46 s) in degrees.

Component	Min	Max	Mean	Std
Yaw	-0.20	0.28	-0.01	0.15
Pitch	-0.29	0.20	-0.14	0.18
Roll	-1.97	0.79	-0.88	0.74

It can be seen that, while the general trajectories of the RW commands are smoother than those of the AI-based controller, the steady-state error is larger. Since no fine-tuning of the PD controller was performed after launch, we assume that the performance could further be improved. This tuning has to be done based on maneuver telemetry data after launch, which can also be done for the AI-based controller. A comparison of the maximum performance of both controllers however was out of scope of the current analyses and is subject to future work.

3.2.3. Comparison with the PD Controller for Diverse Maneuvers

Experiments were conducted using a list of quaternions for both the flight-agent and the PD controller. As with the previous experiments, for the first maneuver the attitude and rates at the experiment start were unmodified and the goal attitude (1, 0, 0, 0) commanded. For the remaining maneuvers, the current attitude was set to a specified quaternion (in this case, one from Table 21), and the goal attitude (1, 0, 0, 0) was commanded, with the initial satellite body rates near 0. For this experiment, the delay between two consecutive maneuvers was increased to 150 s so that distant attitude can be attained and steady-state periods recorded. Since the experiment duration is restricted to 15 minutes due to safety and power constraints, only six maneuvers can be performed with the 150 s delay.

Table 21: List of Initial Commanded Quaternions (rounded to 4 decimal places).

Maneuver	Commanded Quaternion (q_0, q_1, q_2, q_3)
Maneuver 1	variable init. attitude/rates (see below)
Maneuver 2	(0.354, 0.612, -0.354, -0.612)
Maneuver 3	(0.008, -0.087, -0.087, 0.992)
Maneuver 4	(-0.5, -0.5, -0.5, -0.5)
Maneuver 5	(-0.16, 0.066, -0.377, -0.91)
Maneuver 6	(0.0, -0.009, -0.009, 1.0)

For the first maneuver, the initial attitude was $(0.906, -0.0976, 0.0253, -0.410)$ and the initial satellite body rates $(-0.822, -0.0569, -3.53)^\circ/\text{s}$. The Figures 20–23 show the attitude quaternions, commanded RW torques, reaction wheel speeds and satellite body rates, together with the maneuver start and steady-state start times for the LeLaR experiment from December 15, 2025.

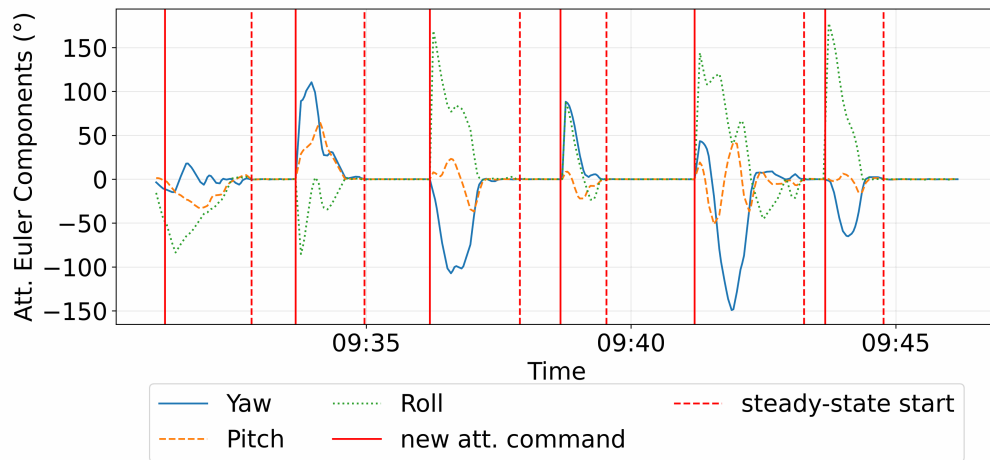


Figure 20: Attitude quaternion for six LeLaR maneuvers from commanded attitude to steady-state start on 2025-12-15. Maneuver 1: 09:31:12–09:32:50 (98 s), Maneuver 2: 09:33:40–09:34:58 (78 s), Maneuver 3: 09:36:12–09:37:54 (102 s), Maneuver 4: 09:38:40–09:39:32 (52 s), Maneuver 5: 09:41:12–09:43:16 (124 s), Maneuver 6: 09:43:40–09:44:46 (66 s).

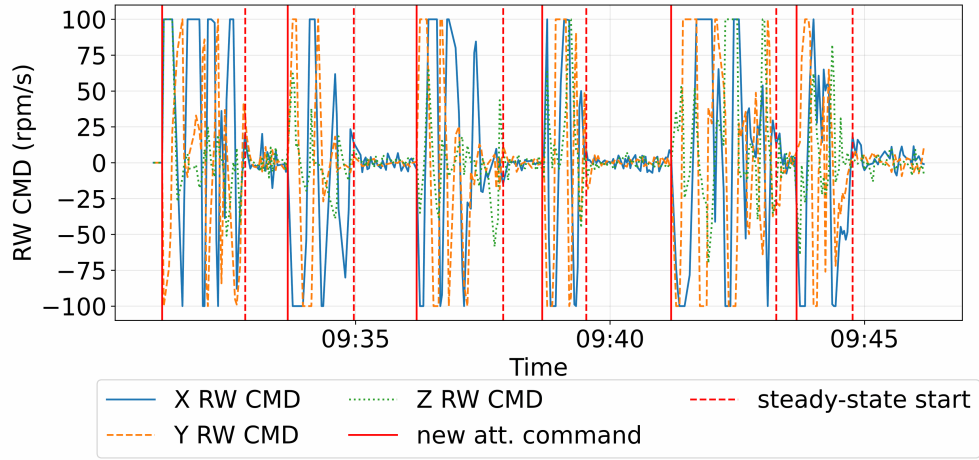


Figure 21: Commanded reaction wheel torques during six LeLaR maneuvers from commanded attitude to steady-state start on 2025-12-15. For the timestamps see Figure 20.

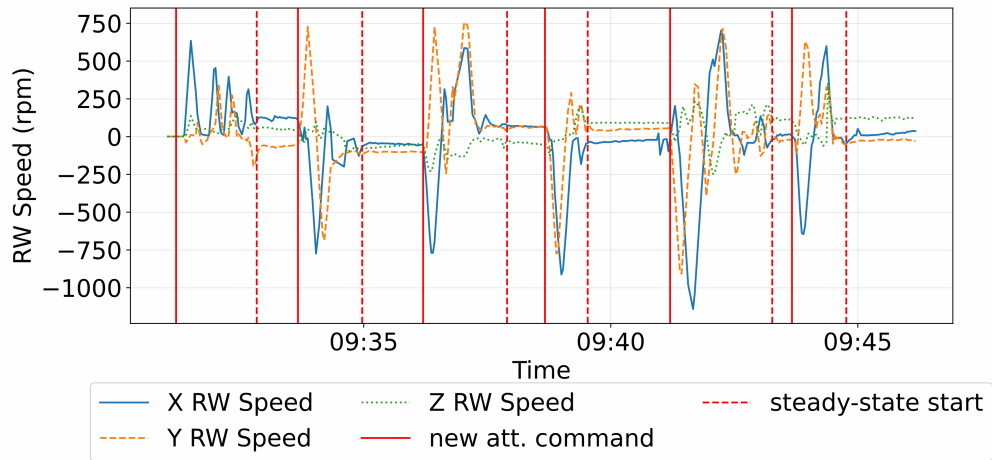


Figure 22: Reaction wheel speeds during six LeLaR maneuvers from commanded attitude to steady-state start on 2025-12-15. For the timestamps see Figure 20.

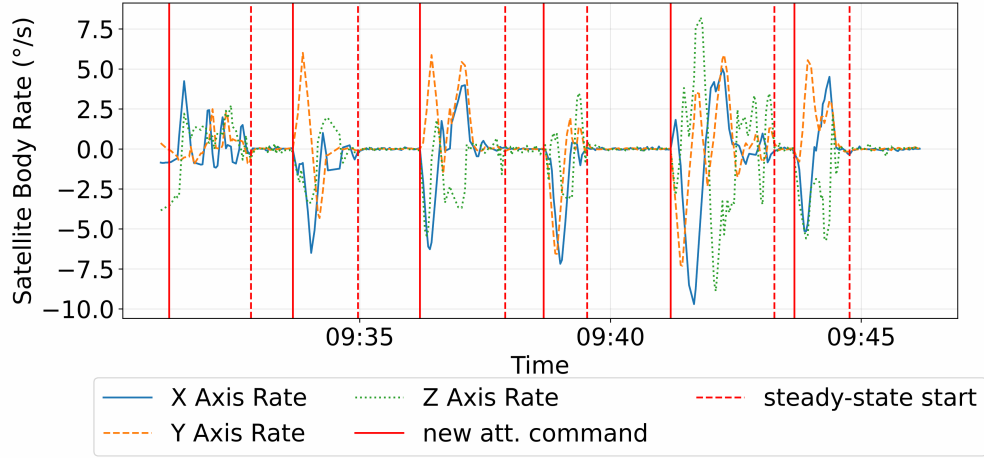


Figure 23: Satellite body rates during six LeLaR maneuvers from commanded attitude to steady-state start on 2025-12-15. For the timestamps see Figure 20.

The Tables 22–27 quantify the steady-state behavior of the maneuvers.

Table 22: Yaw, Pitch, Roll Error - Maneuver 1: Steady-state error statistics from 2025-12-15 09:32:50 to 2025-12-15 09:33:40 (50 s) in degrees.

Component	Min	Max	Mean	Std
Yaw	-0.34	0.21	-0.05	0.15
Pitch	-0.24	0.30	0.00	0.12
Roll	-0.39	0.27	0.01	0.20

Table 23: Yaw, Pitch, Roll Error - Maneuver 2: Steady-state error statistics from 2025-12-15 09:34:58 to 2025-12-15 09:36:12 (74 s) in degrees.

Component	Min	Max	Mean	Std
Yaw	-0.03	0.15	0.07	0.05
Pitch	-0.06	0.09	0.02	0.04
Roll	-0.38	0.07	-0.09	0.09

Table 24: Yaw, Pitch, Roll Error - Maneuver 3: Steady-state error statistics from 2025-12-15 09:37:54 to 2025-12-15 09:38:40 (46 s) in degrees.

Component	Min	Max	Mean	Std
Yaw	-0.05	0.34	0.02	0.09
Pitch	-0.16	0.09	0.00	0.07
Roll	-0.86	0.57	0.03	0.29

Table 25: Yaw, Pitch, Roll Error - Maneuver 4: Steady-state error statistics from 2025-12-15 09:39:32 to 2025-12-15 09:41:12 (100 s) in degrees.

Component	Min	Max	Mean	Std
Yaw	-0.20	0.13	-0.02	0.07
Pitch	-0.78	0.17	-0.02	0.13
Roll	-0.19	0.15	0.01	0.08

Table 26: Yaw, Pitch, Roll Error - Maneuver 5: Steady-state error statistics from 2025-12-15 09:43:16 to 2025-12-15 09:43:40 (24 s) in degrees.

Component	Min	Max	Mean	Std
Yaw	-0.28	0.04	-0.08	0.10
Pitch	-0.09	0.68	0.21	0.27
Roll	-0.65	0.88	0.09	0.37

Table 27: Yaw, Pitch, Roll Error - Maneuver 6: Steady-state error statistics from 2025-12-15 09:44:46 to 2025-12-15 09:46:10 (84 s) in degrees.

Component	Min	Max	Mean	Std
Yaw	-0.39	0.38	-0.06	0.14
Pitch	-0.18	0.42	0.00	0.12
Roll	-0.67	0.45	-0.03	0.21

The same list of quaternions was applied for the classical PD controller of InnoCube. For the first maneuver, the initial attitude was (0.804, 0.0414, 0.0208, 0.593) and the initial satellite body rates were (0.409, 0.102, 5.57) °/s. The goal steady-state was attained only in maneuvers 1 and 5. Figures 24–27 show the PD maneuvers from the experiment from

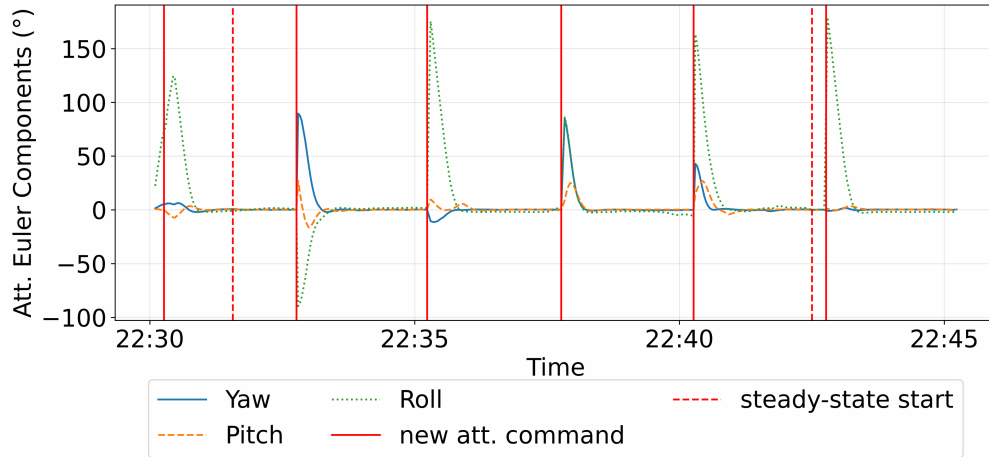


Figure 24: Attitude quaternion for six PD maneuvers from commanded attitude to steady-state start on 2025-12-15. Given a steady-state limit of 1° for each axis, the steady-state was only attained in two maneuvers. The first maneuver was from 22:30:16 to 22:31:34 (78 s) and the fifth maneuver was from 22:40:16 to 22:42:30 (134 s). The other maneuver start times were: Maneuver 2 - 22:32:46, Maneuver 3 - 22:35:14, Maneuver 4 - 22:37:46, Maneuver 6 - 22:42:46.

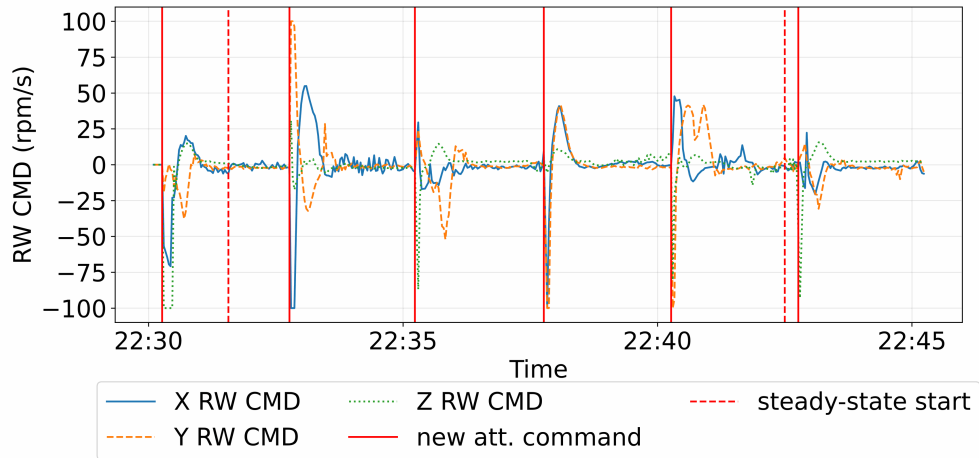


Figure 25: Commanded reaction wheel torques during six PD maneuvers from commanded attitude to steady-state start on 2025-12-15. For the timestamps see Figure 24

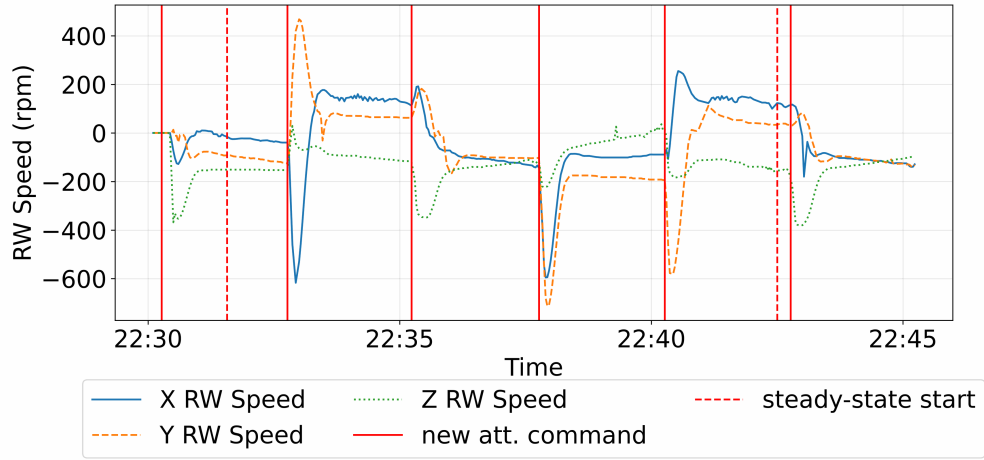


Figure 26: Reaction wheel speeds during six PD maneuvers from commanded attitude to steady-state start on 2025-12-15. For the timestamps see Figure 24

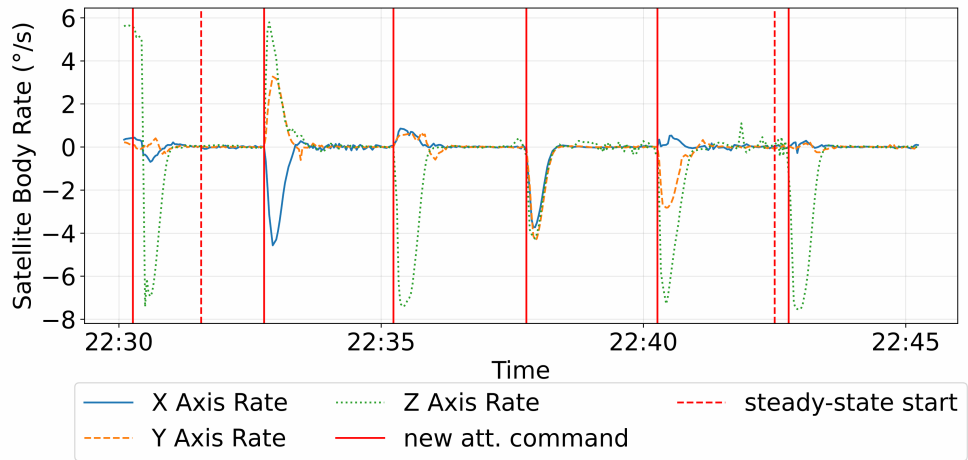


Figure 27: Satellite body rates during six PD maneuvers from commanded attitude to steady-state start on 2025-12-15. For the timestamps see Figure 24

Table 28 and Table 29 quantify the steady-state periods of maneuver 1 and 5.

Table 28: Yaw, Pitch, Roll Error - Maneuver 1: Steady-state error statistics from 2025-12-15 22:31:34 to 2025-12-15 22:32:46 (72 s) in degrees.

Component	Min	Max	Mean	Std
Yaw	0.05	0.74	0.23	0.18
Pitch	0.28	0.40	0.35	0.03
Roll	-0.94	1.67	0.72	0.84

Table 29: Yaw, Pitch, Roll Error - Maneuver 2: Steady-state error statistics from 2025-12-15 22:42:30 to 2025-12-15 22:42:46 (16 s) in degrees

Component	Min	Max	Mean	Std
Yaw	-0.12	0.26	0.13	0.12
Pitch	-0.13	0.23	0.06	0.13
Roll	-0.14	0.52	0.18	0.21

Overall the LeLaR AI-based attitude controller was able to reliably perform inertial pointing attitude control maneuvers, although the boundary conditions in simulation deviated from the actual environment in orbit, demonstrating a successful Sim2Real transfer. The agent also proved adaptable to new safety constraints through post-training, highlighting its flexibility to changing operation scenarios. During in-orbit maneuvers, the steady-state errors were consistently below 1° for all axes. No failure of the flight-agent was observed that would have triggered intervention by the Safety Cage. The results indicate that the LeLaR controller was able to successfully learn and execute attitude control, providing a promising approach for future autonomous spacecraft operations.

4. Conclusions

In this work we have presented the architecture, training procedure and performance of LeLaR, the worlds first AI-based attitude controller successfully tested in orbit. The results show the AI agents ability to reliably perform inertial pointing attitude control maneuvers under real-world conditions. The LeLaR controller shows potential for expansion to more complex scenarios and applications, in particular adaption to a wider range of unexpected deviations from the expected boundary conditions. Short term future work targets the extension of the 15 minute experiment timeframe to allow for the

testing of AI-based momentum management. It would further be of interest to investigate the maximal performance achievable with an AI-based attitude controller by utilizing telemetry data to augment the simulation to better fit the system behavior in orbit, including the RW and residual magnetic dipole compensation discrepancies that are currently still present. In that sense we will investigate the optimization of the balance between target achievement and constraint satisfaction, like adhering to rate limits, and compare the AI-based attitude controller with fine-tuned classical controllers, like PD and SMC controllers. We want to further improve and generalize the development of AI-based attitude controllers. We aim for a system that allows for the provision of a system specification and an optimization target (e.g., attitude control mode, limits and constraints, etc.) so that an appropriate controller can be derived automatically. We believe such a system can be included in general mission planning as the system specification and targets are available for the mission related simulations. Besides this, we intend to transfer the AI-based attitude controller to other satellites. The controller was designed as a drop-in replacement for the PD controller of InnoCube and, as such, does not impose demanding hardware requirements or exceed the interface complexity of classical attitude controllers. Retrofitting an existing ADCS system would require enabling data provision and integration into the existing watchdog architecture (e.g., the Safety Cage if available). Our long-term goal is to train a collection of base-agents for different satellite configurations that can be deployed to new systems and autonomously fine-tune themselves during the commissioning phase in-orbit.

CRedit Authorship Contribution Statement

Kirill Djebko, Sergio Montenegro, Frank Puppe: Conceptualization; Kirill Djebko, Tom Baumann: Data curation; Kirill Djebko, Tom Baumann: Formal analysis; Sergio Montenegro, Frank Puppe: Funding acquisition; Kirill Djebko, Tom Baumann, Erik Dilger: Investigation; Kirill Djebko, Tom Baumann: Methodology; Kirill Djebko, Sergio Montenegro: Project administration; Sergio Montenegro, Frank Puppe: Resources; Kirill Djebko, Tom Baumann: Software; Sergio Montenegro, Frank Puppe: Supervision; Kirill Djebko, Tom Baumann: Validation; Kirill Djebko, Tom Baumann: Visualization; Kirill Djebko, Tom Baumann, Erik Dilger, Sergio Montenegro, Frank Puppe: Roles/Writing - original draft; Kirill Djebko, Tom Baumann, Erik Dilger, Sergio Montenegro, Frank Puppe: Writing - review & editing.

Acknowledgments

This work was conducted as part of the “In-Orbit-Demonstrator Lernende Lageregelung (LeLaR)” project (grant number/FKZ: 50RA2403), funded by the German Federal Ministry for Economic Affairs and Energy (Bundesministerium für Wirtschaft und Energie, BMWE) on the basis of a decision by the German Bundestag.

Conflicts of Interest

The authors declare no conflicts of interest. The funders had no role in the design of the study; in the collection, analyses, or interpretation of data; in the writing of the manuscript; or in the decision to publish the results.

Data Availability

The maneuver telemetry datasets generated and analyzed during this work are available in the GitHub repository <https://github.com/kdjebko/lelar-in-orbit-data>.

References

- [1] N. Rudin, D. Hoeller, P. Reist, M. Hutter, Learning to walk in minutes using massively parallel deep reinforcement learning, CoRR abs/2109.11978 (2021). arXiv:2109.11978.
URL <https://arxiv.org/abs/2109.11978>
- [2] L. Röstel, D. Winkelbauer, J. Pitz, L. Sievers, B. Bäuml, Composing dextrous grasping and in-hand manipulation via scoring with a reinforcement learning critic, in: 2025 IEEE International Conference on Robotics and Automation (ICRA), IEEE, 2025, p. 11683–11690. doi:10.1109/icra55743.2025.11127792.
URL <http://dx.doi.org/10.1109/ICRA55743.2025.11127792>
- [3] S. Zhou, H. Yang, S. Zhang, X. Bai, F. Wang, Sac-based intelligent load relief attitude control method for launch vehicles, Aerospace 12 (3) (2025). doi:10.3390/aerospace12030203.
URL <https://www.mdpi.com/2226-4310/12/3/203>

- [4] S. Xue, H. Bai, D. Zhao, J. Zhou, Research on intelligent control method of launch vehicle landing based on deep reinforcement learning, *Mathematics* 11 (20) (2023) 4276. doi:10.3390/math11204276.
URL <https://doi.org/10.3390/math11204276>
- [5] T. Hörger, K. Dresia, G. Waxenegger-Wilfing, S. Schlechtriem, Machine learning based combustion chamber pressure and mixture ratio controller – simulative and experimental evaluation of control performance, in: *AIAA SCITECH 2025 Forum*, 2025, p. 2636. doi:10.2514/6.2025-2636.
URL <https://doi.org/10.2514/6.2025-2636>
- [6] J. He, B. Ren, Y. Xu, Q. Zhao, S. Du, B. Wang, Neural network adaptive attitude control of full-states quad tiltrotor uav, *Aerospace* 12 (8) (2025). doi:10.3390/aerospace12080684.
URL <https://www.mdpi.com/2226-4310/12/8/684>
- [7] M. B. Mohiuddin, I. Boiko, V. P. Tran, M. Garratt, A. Abdallah, Y. Zweiri, Reinforcement learning for end-to-end uav slung-load navigation and obstacle avoidance, *Scientific Reports* 15 (2025) 34621. doi:10.1038/s41598-025-18220-6.
URL <https://doi.org/10.1038/s41598-025-18220-6>
- [8] M. Willoughby, K. Richelmy, H. Peng, Satellite Reorientation Using Reinforcement Learning Under Unknown Attitude Failure: Sun-Searching Implementation. arXiv:<https://arc.aiaa.org/doi/pdf/10.2514/6.2025-1145>, doi:10.2514/6.2025-1145.
URL <https://arc.aiaa.org/doi/abs/10.2514/6.2025-1145>
- [9] Á. G. Pérez Muñoz, G. López García, I. García Villoria, A. A. Alonso Muñoz, Á. L. Porrás Hermoso, M. d. l. S. Pérez Hernández, Feasibility of deep reinforcement learning for the real-time attitude control of a satellite system, *Journal of Systems Architecture* 167 (103513), *sistemas de tiempo real y arquitectura de servicios telemáticos STRAST* (July 2025). doi:10.1016/j.sysarc.2025.103513.
URL <https://www.sciencedirect.com/science/article/pii/S1383762125001857?via%3Dihub>
- [10] W. Retagne, J. Dauer, G. Waxenegger-Wilfing, Adaptive satellite atti-

- tude control for varying masses using deep reinforcement learning, *Frontiers in Robotics and AI* 11 (2024) 1402846.
- [11] R. S. Sutton, and A. G. Barto, Reinforcement learning: An introduction, no. 1, MIT press Cambridge, 1998.
 - [12] T. Haarnoja, A. Zhou, P. Abbeel, S. Levine, Soft actor-critic: Off-policy maximum entropy deep reinforcement learning with a stochastic actor, in: *International conference on machine learning*, Pmlr, 2018, pp. 1861–1870.
 - [13] T. P. Lillicrap, J. J. Hunt, A. Pritzel, N. Heess, T. Erez, Y. Tassa, D. Silver, D. Wierstra, Continuous control with deep reinforcement learning, *arXiv preprint arXiv:1509.02971* (2015).
 - [14] J. Schulman, F. Wolski, P. Dhariwal, A. Radford, O. Klimov, Proximal policy optimization algorithms, *arXiv preprint arXiv:1707.06347* (2017).
 - [15] K. Djebko, F. Puppe, S. Montenegro, T. Baumann, and M. Faisal, Learning attitude control, in: *Proceedings of the 14th IAA Symposium on Small Satellites for Earth System Observation*, Berlin, Germany, 2023, presented at the 14th IAA Symposium on Small Satellites for Earth System Observation, May 7–12, 2023.
 - [16] M. Carrillo Barrenechea, P. Lachevre, I. Karsli Terjan, M. Watt, C. Hervas Garcia, Enabling ai-in-the-loop aocs algorithms on in-flight hardware: from conception to in-orbit demonstration in ESA OPS-SAT, in: *Proceedings of the 12th ESA Guidance, Navigation & Control Conference*, ESA, 2023, pp. Sopot, Poland. doi:10.5270/esa-gnc-icatt-2023-131.
 - [17] Airbus Defence and Space, HOPAS on OPS-SAT - executive summary, ESA Contract Report 4000137215/22/NL/GLC/ov, European Space Agency (ESA), implemented as ESA OSIP; Publishing Date: 7 December 2022 (dec 2022).
 - [18] R. Gerlich, R. Gerlich, S. Montenegro, F. Puppe, K. Djebko, C. Plasberg, and M. Bädorf, It’s the data, stupid! constructive and analytical quality-assurance for ai-based space systems, presented at *DASIA 2023*, June 6–8, Sitges, Spain, 2023.

- [19] K. Djebko, T. Baumann, E. Dilger, F. Puppe, and S. Montenegro, Ai-based attitude control for restricted reaction wheels, in: Proceedings of the 15th IAA Symposium on Small Satellites for Earth System Observation, Berlin, Germany, 2025, presented at the 15th IAA Symposium on Small Satellites for Earth System Observation, May 4–8, 2025.
- [20] B. Grzesik, T. Baumann, T. Walter, F. Flederer, E. Dilger, F. Sittner, S. Gläsner, J. L. Kirchler, M. Tedsen, S. Montenegro, and E. Stoll, Innocube—a wireless satellite platform to demonstrate innovative technologies, *Aerospace* 8 (5) (2021). doi:10.3390/aerospace8050127. URL <https://www.mdpi.com/2226-4310/8/5/127>
- [21] S. Montenegro, T. Baumann, E. Dilger, F. Sittner, M. Strohmaier, T. Walter, and S. Gläsner, InnoCube: Der erste drahtloser Satellit, Deutsche Gesellschaft für Luft- und Raumfahrt - Lilienthal-Oberth e.V.URN: urn:nbn:de:101:1-2022111811082499997154 (2022). doi:10.25967/570007.
- [22] T. Baumann, E. Dilger, S. Montenegro, F. Sittner, M. Arbab, and T. Walter, InnoCube – First In-Orbit Results of the Fully Wireless Satellite Data Bus, in: Proceedings of SmallSat 2025, Salt Lake City, USA, presented at SmallSat 2025, August 10–13, 2025. doi:10.26077/956f-62d3.
- [23] S. Tsimenidis, Limitations of deep neural networks: a discussion of g. marcus’ critical appraisal of deep learning, arXiv preprint arXiv:2012.15754 (2020). URL <https://arxiv.org/abs/2012.15754>
- [24] K. Djebko, T. Baumann, E. Dilger, F. Puppe, S. Montenegro, Vereinigung der steuerung von aktuatoren mit unterschiedlichen zeithorizonten für ki-basierte satelliten-lageregelung mittels subnetz-politik, in: Deutscher Luft- und Raumfahrtkongress 2025, Deutsche Gesellschaft für Luft- und Raumfahrt - Lilienthal-Oberth e.V., Bonn, 2025, p. 10. doi:10.25967/650051. URL <https://doi.org/10.25967/650051>
- [25] Silicon Labs, EFR32FG12 Gecko datasheet Rev. 1.8, <https://www.silabs.com/documents/public/data-sheets/efr32fg12-datasheet.pdf>, last visited December 18, 2025 (2022).

- [26] STMicroelectronics, ASM330LHH Automotive 6-axis inertial module datasheet, <https://www.st.com/resource/en/datasheet/asm330lhh.pdf>, last visited December 18, 2025 (2020).
- [27] PNI Sensor, RM3100 Geomagnetic Sensor datasheet, https://www.unitronic.de/wp-content/uploads/2025/12/21093_DB_RM3100.pdf, last visited December 18, 2025 (2020).
- [28] Celestrak, SatCat Table: INNOCUBE, <https://celestrak.org/satcat/table-satcat.php?NAME=INNOCUBE>, last visited February 14, 2025 (2025).
- [29] S. Busch, P. Bangert, S. Dombrovski and K. Schilling, Uwe-3, in-orbit performance and lessons learned of a modular and flexible satellite bus for future pico-satellite formations, *Acta Astronautica* 117 (2015) 73–89. doi:doi.org/10.1016/j.actaastro.2015.08.002.
URL <https://www.sciencedirect.com/science/article/pii/S0094576515003185>
- [30] A. Paszke, S. Gross, F. Massa, A. Lerer, J. Bradbury, G. Chanan, T. Killeen, Z. Lin, N. Gimelshein, L. Antiga, A. Desmaison, A. Köpf, E. Yang, Z. DeVito, M. Raison, A. Tejani, S. Chilamkurthy, B. Steiner, L. Fang, J. Bai, S. Chintala, Pytorch: An imperative style, high-performance deep learning library, arXiv preprint arXiv:1912.01703 (2019).
URL <https://arxiv.org/abs/1912.01703>
- [31] ECSS Secretariat Requirements & Standards Section, Space engineering - machine learning handbook, ECSS-E-HB-40-02A (2024).